Supporting Information:

Nonadiabatic Field with Triangle Window

Functions on Quantum Phase Space

Xin He, Xiangsong Cheng, Baihua Wu, and Jian Liu*

Beijing National Laboratory for Molecular Sciences, Institute of Theoretical and Computational

Chemistry, College of Chemistry and Molecular Engineering,

Peking University, Beijing 100871, China

AUTHOR INFORMATION

Corresponding Author

* Electronic mail: jianliupku@pku.edu.cn

S1: Proof that the CPS-TW Expression of the Time Correlation Function Involving Coherence Terms is Exact for Electronic Dynamics of the Pure *F*-State Quantum System

In the literature, when $n \neq m$, $|n\rangle\langle m|$ is also denoted as a coherence term, and $|n\rangle\langle n|$ represents a population term. In the four kinds of time correlation functions of electronic degrees of freedom (DOFs), while only the population-population correlation function does not involve any coherence terms, all of the other three kinds include coherence terms. As proved in ref [1], the CPS-TW expression for the population-population correlation function, which includes eqs (11)-(17) of the main text (of the present letter), is exact for the pure two-state quantum system. Although it is not exact for the population dynamics of the pure *F*-state quantum system when $F \geq 3$, the numerical performance is reasonably good. Below we focus on the CPS-TW expressions for the three kinds of time correlation functions involving coherence terms, which are eqs (10), (12), (14)-(15) and (18)-(21) of the main text.

Consider the pure *F*-electronic-state system, i.e., the frozen nuclei-limit of the Hamiltonian of eq (1) of the main text, which reads $\hat{H} = \sum_{n,m=1}^{F} H_{nm} |n\rangle\langle m|$. Here, H_{nm} is set as the constant element in the *n*-th row and *m*-th column of the $F \times F$ Hermitian matrix **H**. (When only electronic DOFs are involved, the convention $\hbar = 1$ is adopted.) For simplicity, following ref [2] of Cotton and Miller, we define the action variables $\{\mathbf{e}\}$ and angle variables $\{\boldsymbol{\theta}\}$ as

$$
\begin{aligned}
e^{(k)} &= \frac{1}{2}\left(\left(x^{(k)}\right)^2 + \left(p^{(k)}\right)^2\right) \\
\theta^{(k)} &= \arctan\left(p^{(k)}/x^{(k)}\right)
\end{aligned} \qquad (S1)
$$

We utilize the transformation between coordinate-momentum variables and action-angle variables, eq (S1), to obtain the expression of the population-coherence correlation function (where $k \neq l$):

$$\text{Tr}_e\left[|n\rangle\langle n|e^{i\hat{H}t}|k\rangle\langle l|e^{-i\hat{H}t}\right]$$

$$\mapsto \int \frac{2d\mathbf{x}_0 d\mathbf{p}_0}{(2\pi)^F \left(2-\frac{1}{2}\left(\left(x_0^{(n)}\right)^2+\left(p_0^{(n)}\right)^2\right)\right)^{F-2}} K_{nn}^{\text{SQC}}\left(\mathbf{x}_0,\mathbf{p}_0\right)K_{lk}^{\text{CMM}}\left(\mathbf{x}_t,\mathbf{p}_t\right)\ , \qquad (S2)$$

$$=\int \frac{2d\mathbf{e}_0 d\mathbf{\theta}_0}{(2\pi)^F \left(2-e_0^{(n)}\right)^{F-2}} K_{nn}^{\text{SQC}}\left(\mathbf{e}_0,\mathbf{\theta}_0\right)K_{lk}^{\text{CMM}}\left(\mathbf{e}_t,\mathbf{\theta}_t\right)$$

where

$$K_{nn}^{\text{SQC}}\left(\mathbf{e},\mathbf{\theta}\right)\equiv K_{nn}^{\text{SQC}}\left(\mathbf{e}\right)=h\left(e^{(n)}-1\right)\prod_{n'\neq n}h\left(2-e^{(n)}-e^{(n')}\right) \qquad (S3)$$

and

$$K_{lk}^{\text{CMM}}\left(\mathbf{e},\mathbf{\theta}\right)=\sqrt{e^{(l)}e^{(k)}}e^{i(\theta^{(l)}-\theta^{(k)})} \qquad (S4)$$

are derived from substitution of eq (S1) into eqs (14)-(15) and eq (19) of the main text.

For $n\neq m$, the expression of the coherence-population or coherence-coherence correlation function reads

$$\text{Tr}_e\left[|n\rangle\langle m|e^{i\hat{H}t}|k\rangle\langle l|e^{-i\hat{H}t}\right]$$

$$\mapsto \int \frac{12d\mathbf{x}_0 d\mathbf{p}_0}{5(2\pi)^F}\sum_{i=n,m}\frac{K_{ii}^{\text{SQC}}\left(\mathbf{x}_0,\mathbf{p}_0\right)}{\left(2-\frac{1}{2}\left(\left(x_0^{(i)}\right)^2+\left(p_0^{(i)}\right)^2\right)\right)^{F-2}}K_{mn}^{\text{CMM}}\left(\mathbf{x}_0,\mathbf{p}_0\right)K_{lk}^{\text{CMM}}\left(\mathbf{x}_t,\mathbf{p}_t\right)\ . \qquad (S5)$$

$$=\int \frac{12d\mathbf{e}_0 d\mathbf{\theta}_0}{5(2\pi)^F}\sum_{i=n,m}\frac{K_{ii}^{\text{SQC}}\left(\mathbf{e}_0,\mathbf{\theta}_0\right)}{\left(2-e_0^{(i)}\right)^{F-2}}K_{mn}^{\text{CMM}}\left(\mathbf{e}_0,\mathbf{\theta}_0\right)K_{lk}^{\text{CMM}}\left(\mathbf{e}_t,\mathbf{\theta}_t\right)$$

In comparison, for general $n,m,k,l\in\{1,\cdots,F\}$, the exact time correlation function reads

$$\text{Tr}_e\left[|n\rangle\langle m|e^{i\hat{H}t}|k\rangle\langle l|e^{-i\hat{H}t}\right]=U_{ln}(t)U_{km}^*(t), \qquad (S6)$$

where the time evolution operator $e^{-i\hat{H}t}$ is represented by a $F\times F$ unitary matrix $\mathbf{U}(t)=e^{-i\mathbf{H}t}$.

We prove that the correlation function defined by eq (S2) or eq (S5) for electronic DOFs is exact, when the equations of motion (EOMs) of mapping electronic variables are

$$\dot{\mathbf{g}} = -i\mathbf{H}\mathbf{g}, \tag{S7}$$

which leads to the solution of $\mathbf{g}_t$,

$$\mathbf{g}_t = \mathbf{U}(t)\mathbf{g}_0 \equiv e^{-i\mathbf{H}t}\mathbf{g}_0. \tag{S8}$$

Equation (S7) is isomorphic to the time-dependent Schrödinger equation. Following eq (S8), the time evolution of off-diagonal (i.e., $l \neq k$) elements of the CMM kernel reads

$$
\begin{aligned}
K_{lk}^{\mathrm{CMM}}(\mathbf{e}_t, \mathbf{\theta}_t) &= K_{lk}^{\mathrm{CMM}}(\mathbf{x}_t, \mathbf{p}_t) \\
&= \frac{1}{2}\left(x_t^{(l)} + ip_t^{(l)}\right)\left(x_t^{(k)} - ip_t^{(k)}\right) \\
&= \frac{1}{2}\left(\mathbf{U}(t)\mathbf{g}_0\right)_l \left(\mathbf{g}_0^\dagger \mathbf{U}^\dagger(t)\right)_k \\
&= \sum_{r,s=1}^{F} U_{lr}(t) U_{ks}^*(t) \sqrt{e_0^{(r)} e_0^{(s)}}\, e^{i\left(\theta_0^{(r)} - \theta_0^{(s)}\right)}
\end{aligned}
\tag{S9}
$$

1) The Proof of the Exact *Population-Coherence* Correlation Function for Electronic Dynamics of the Pure *F*-State Quantum System

When only electronic DOFs are involved, by using eq (S9), and also utilizing that for any $\theta_0^{(k)}, k = 1, \ldots, F$, and integer m,

$$\int_0^{2\pi} e^{im\theta_0^{(k)}}\, \mathrm{d}\theta_0^{(k)} = 2\pi\delta_{m0} = \delta_{m0}\int_0^{2\pi} \mathrm{d}\theta_0^{(k)}, \tag{S10}$$

it is straight-forward to show the population-coherence correlation function eq (S2) leads to

$$
\begin{aligned}
&\int \frac{2\mathrm{d}\mathbf{e}_0 \mathrm{d}\mathbf{\theta}_0}{(2\pi)^F \left(2 - e_0^{(n)}\right)^{F-2}} K_{nn}^{\mathrm{SQC}}(\mathbf{e}_0, \mathbf{\theta}_0) K_{lk}^{\mathrm{CMM}}(\mathbf{e}_t, \mathbf{\theta}_t) \\
&= \int \frac{2\mathrm{d}\mathbf{e}_0 \mathrm{d}\mathbf{\theta}_0}{(2\pi)^F \left(2 - e_0^{(n)}\right)^{F-2}} K_{nn}^{\mathrm{SQC}}(\mathbf{e}_0) \sum_{r,s=1}^{F} U_{lr}(t) U_{ks}^*(t) \sqrt{e_0^{(r)} e_0^{(s)}}\, e^{i\left(\theta_0^{(r)} - \theta_0^{(s)}\right)}. \\
&= \int \frac{2\mathrm{d}\mathbf{e}_0}{\left(2 - e_0^{(n)}\right)^{F-2}} K_{nn}^{\mathrm{SQC}}(\mathbf{e}_0) \sum_{r=1}^{F} U_{lr}(t) U_{kr}^*(t) e_0^{(r)}
\end{aligned}
\tag{S11}
$$

Then, using the properties that for $l \neq k$, $\sum_{r=1}^{F} U_{lr}(t)U_{kr}^{*}(t) = 0$ and that for any $r \neq s \neq n$,

$$\int \frac{2d\mathbf{e}}{\left(2-e^{(n)}\right)^{F-2}} K_{nn}^{\text{SQC}}(\mathbf{e})e^{(r)} = \int \frac{2d\mathbf{e}}{\left(2-e^{(n)}\right)^{F-2}} K_{nn}^{\text{SQC}}(\mathbf{e})e^{(s)} , \tag{S12}$$

eq (S11) is transformed to

$$\int \frac{2d\mathbf{e}_0}{\left(2-e_0^{(n)}\right)^{F-2}} K_{nn}^{\text{SQC}}(\mathbf{e}_0) \sum_{r=1}^{F} U_{lr}(t)U_{kr}^{*}(t)e_0^{(r)}$$

$$= U_{ln}(t)U_{kn}^{*}(t)\int \frac{2d\mathbf{e}_0}{\left(2-e_0^{(n)}\right)^{F-2}} K_{nn}^{\text{SQC}}(\mathbf{e}_0)\left(e_0^{(n)} - e_0^{(r \neq n)}\right) \tag{S13}$$

In ref [2] Cotton and Miller obtained the following integrals,

$$\int \frac{2d\mathbf{e}}{\left(2-e^{(n)}\right)^{F-2}} K_{nn}^{\text{SQC}}(\mathbf{e})e^{(n)}$$

$$= \int_{1}^{2} 2de^{(n)}e^{(n)}\left(2-e^{(n)}\right)^{2-F} \prod_{n' \neq n}\int_{0}^{2-e^{(n)}} de^{(n')} , \tag{S14}$$

$$= \frac{4}{3}$$

and

$$\int \frac{2d\mathbf{e}}{\left(2-e^{(n)}\right)^{F-2}} K_{nn}^{\text{SQC}}(\mathbf{e})e^{(r \neq n)}$$

$$= \int_{1}^{2} 2de^{(n)}\left(2-e^{(n)}\right)^{2-F} \int_{0}^{2-e^{(n)}} de^{(r)}e^{(r)} \prod_{n' \neq \{n,r\}}\int_{0}^{2-e^{(n)}} de^{(n')} . \tag{S15}$$

$$= \frac{1}{3}$$

Substitution of eqs (S14) and (S15) into eq (S13) yields

S4

$$\int \frac{2\mathrm{d}\mathbf{e}_0\mathrm{d}\boldsymbol{\theta}_0}{(2\pi)^F \left(2-e_0^{(n)}\right)^{F-2}} K_{nn}^{\mathrm{SQC}}\left(\mathbf{e}_0,\boldsymbol{\theta}_0\right) K_{lk}^{\mathrm{CMM}}\left(\mathbf{e}_t,\boldsymbol{\theta}_t\right)$$

$$= U_{ln}(t)U_{kn}^*(t)\left(\frac{4}{3}-\frac{1}{3}\right) \tag{S16}$$

$$= \mathrm{Tr}\left[|n\rangle\langle n|e^{i\hat{H}t}|k\rangle\langle l|e^{-i\hat{H}t}\right]$$

Thus, eq (S2), the expression of the population-coherence correlation function, reproduces the exact result of the pure F-electronic-state system.

2) The Proof of the Exact *Coherence-Population* Correlation Function and *Coherence-Coherence* Correlation Function for Electronic Dynamics of the Pure F-State Quantum System

Utilizing eqs (S9)-(S10), for eq (S5) with $n \neq m$, we obtain

$$\int \frac{12\mathrm{d}\mathbf{e}_0\mathrm{d}\boldsymbol{\theta}_0}{5(2\pi)^F} \sum_{i=n,m} \frac{K_{ii}^{\mathrm{SQC}}\left(\mathbf{e}_0,\boldsymbol{\theta}_0\right)}{\left(2-e_0^{(i)}\right)^{F-2}} K_{mn}^{\mathrm{CMM}}\left(\mathbf{e}_0,\boldsymbol{\theta}_0\right) K_{lk}^{\mathrm{CMM}}\left(\mathbf{e}_t,\boldsymbol{\theta}_t\right)$$

$$= \int \frac{12\mathrm{d}\mathbf{e}_0\mathrm{d}\boldsymbol{\theta}_0}{5(2\pi)^F} \sum_{i=n,m} \frac{K_{ii}^{\mathrm{SQC}}\left(\mathbf{e}_0,\boldsymbol{\theta}_0\right)}{\left(2-e_0^{(i)}\right)^{F-2}} \sqrt{e_0^{(m)}e_0^{(n)}}\, e^{i\left(\theta_0^{(m)}-\theta_0^{(n)}\right)}$$

$$\times \sum_{r,s=1}^F U_{lr}(t)U_{ks}^*(t)\sqrt{e_0^{(r)}e_0^{(s)}}\, e^{i\left(\theta_0^{(r)}-\theta_0^{(s)}\right)} \tag{S17}$$

$$= U_{ln}(t)U_{km}^*(t)\int \frac{12\mathrm{d}\mathbf{e}_0}{5} \sum_{i=n,m} \frac{K_{ii}^{\mathrm{SQC}}\left(\mathbf{e}_0\right)}{\left(2-e_0^{(i)}\right)^{F-2}} e_0^{(m)}e_0^{(n)}$$

we can derive that

$$\int 2\mathrm{d}\mathbf{e}\, \frac{K_{kk}^{\mathrm{SQC}}\left(\mathbf{e}\right)}{\left(2-e^{(k)}\right)^{F-2}} e^{(k)}e^{(j\neq k)}$$

$$= \int_1^2 2\mathrm{d}e^{(k)}e^{(k)}\left(2-e^{(k)}\right)^{2-F} \int_0^{2-e^{(k)}} \mathrm{d}e^{(j)}e^{(j)} \prod_{k'\neq\{j,k\}} \int_0^{2-e^{(k)}} \mathrm{d}e^{(k')} . \tag{S18}$$

$$= \frac{5}{12}$$

By substituting eq (S18) into eq (S17), we obtain

$$
\int \frac{12 \mathrm{d}\mathbf{e}_0 \mathrm{d}\boldsymbol{\theta}_0}{5(2\pi)^F} \sum_{i=n,m} \frac{K_{ii}^{\mathrm{SQC}}(\mathbf{e}_0,\boldsymbol{\theta}_0)}{\left(2-e_0^{(i)}\right)^{F-2}} K_{mn}^{\mathrm{CMM}}(\mathbf{e}_0,\boldsymbol{\theta}_0) K_{lk}^{\mathrm{CMM}}(\mathbf{e}_t,\boldsymbol{\theta}_t)
$$

$$
= U_{ln}(t) U_{km}^*(t) \left(\frac{6}{5} \times 2 \times \frac{5}{12} \right) \qquad , \qquad (S19)
$$

$$
= \mathrm{Tr}\left[|n\rangle\langle m| e^{i\hat{H}t} |k\rangle\langle l| e^{-i\hat{H}t} \right]
$$

so that eq (S5), the expression of the coherence-population correlation function as well as the coherence-coherence correlation function, is also exact for electronic dynamics of the pure F-state quantum system.

S2: Numerical Details in Evaluation of the Time Correlation Function in NaF-TW, NaF and SQC-TW

As discussed in ref [3], in evaluation of the time correlation function of eq (21) of the main text, i.e.,

$$
\mathrm{Tr}_{n,e}\left[\left(|n\rangle\langle m| \otimes \hat{\rho}_{\mathrm{nuc}} \right) e^{i\hat{H}t/\hbar} \left(|k\rangle\langle l| \otimes \hat{A}_{\mathrm{nuc}} \right) e^{-i\hat{H}t/\hbar} \right], \qquad (S20)
$$

trajectory-based quantum dynamics methods involve three key elements: the initial condition, the integral expression of the time correlation function, and the EOMs for trajectories. The main text introduces NaF-TW, which employs the triangle window (TW) functions for electronic DOFs for the time correlation function. In this section, we present numerical details of NaF-TW, NaF and SQC-TW for the three key elements in the phase space formulation.

S2-A: Initial Conditions for NaF-TW, NaF and SQC-TW

The integral expression of the time correlation function of eq (21) in the main text is interpreted as the summation over trajectories with proper initial conditions. The initial value of phase space variables of nuclear DOFs is sampled from the Wigner distribution

$\rho_W(\mathbf{R}, \mathbf{P}) = \int d\boldsymbol{\Delta} \langle \mathbf{R} - \boldsymbol{\Delta}/2 | \hat{\rho}_{\text{nuc}} | \mathbf{R} + \boldsymbol{\Delta}/2 \rangle \exp(-i\boldsymbol{\Delta} \cdot \mathbf{P}/\hbar)$. The sampling procedures of the initial value of phase space variables of electronic DOFs, including coordinate-momentum variables $(\mathbf{x}, \mathbf{p})$ and commutator matrix variables $\boldsymbol{\Gamma}$ in the diabatic representation (or $(\tilde{\mathbf{x}}, \tilde{\mathbf{p}})$ and $\tilde{\boldsymbol{\Gamma}}$ in the adiabatic representation), are separately described for the NaF-TW, NaF and SQC-TW methods.

1) **Initial Value of Coordinate-Momentum Variables $(\mathbf{x}_0, \mathbf{p}_0)$ or $(\tilde{\mathbf{x}}_0, \tilde{\mathbf{p}}_0)$ for Electronic DOFs in NaF**

In NaF, the initial value of $(\mathbf{x}_0, \mathbf{p}_0)$ in the diabatic representation or $(\tilde{\mathbf{x}}_0, \tilde{\mathbf{p}}_0)$ in the adiabatic representation, is uniformly sampled on the corresponding CPS, $\mathcal{S}(\mathbf{x}, \mathbf{p}; \gamma)$ or $\mathcal{S}(\tilde{\mathbf{x}}, \tilde{\mathbf{p}}; \gamma)$. This process includes the following steps:

Step 1: Generate a $2F$-dimensional random vector $\boldsymbol{\xi}$ whose components are independently sampled from the standard normal (Gaussian) distribution, i.e., $\xi^{(k)} \sim \mathcal{N}(0,1)$ with $k = 1, \cdots, 2F$.

Step 2: Normalize the vector $\boldsymbol{\xi}$: for $k = 1, \cdots, 2F$, $\xi_{\text{norm}}^{(k)} = \xi^{(k)} / \sqrt{\sum_{i=1}^{2F} (\xi^{(i)})^2}$.

Step 3: The initial value of coordinate variables is proportional to the value of the first F components of $\boldsymbol{\xi}_{\text{norm}}$, while the initial value of momentum variables is proportional to that of the remaining F components, i.e.,

$$\begin{aligned} x_0^{(k)} &= \sqrt{2(1 + F\gamma)}\xi_{\text{norm}}^{(k)} \\ p_0^{(k)} &= \sqrt{2(1 + F\gamma)}\xi_{\text{norm}}^{(F+k)} \end{aligned} \quad , \quad k = 1, \cdots, F \tag{S21}$$

in the diabatic representation, or similarly

$$\begin{aligned} \tilde{x}_0^{(k)} &= \sqrt{2(1 + F\gamma)}\xi_{\text{norm}}^{(k)} \\ \tilde{p}_0^{(k)} &= \sqrt{2(1 + F\gamma)}\xi_{\text{norm}}^{(F+k)} \end{aligned} \quad , \quad k = 1, \cdots, F \tag{S22}$$

in the adiabatic representation.

2) Initial Value of Coordinate-Momentum Variables $(\mathbf{x}_0, \mathbf{p}_0)$ or $(\tilde{\mathbf{x}}_0, \tilde{\mathbf{p}}_0)$ for Electronic DOFs in NaF-TW or SQC-TW

In either NaF-TW or SQC-TW, the initial sampling procedure of electronic phase space variables $(\mathbf{x}_0, \mathbf{p}_0)$ in the diabatic representation reads:

Step 1: Choose the initially occupied state. When we consider the population-population ($n = m$ and $k = l$) or population-coherence ($n = m$ and $k \neq l$) correlation function, set the occupied state j_{occ} as n. When we calculate the coherence-population ($n \neq m$ and $k = l$) or coherence-coherence ($n \neq m$ and $k \neq l$) correlation function, j_{occ} is randomly assigned to be either of n and m with the equal probability.

Step 2: When the occupied state is j_{occ}, generate the initial value of action-angle variables $\{\mathbf{e}, \mathbf{\theta}\}$ by using the algorithm of Cotton and Miller described in ref[2]. First, iteratively generate two real random numbers ζ and ζ_2 from a uniform distribution on domain $[0,1]$ until their sum $\zeta + \zeta_2 < 1$, and record the value of ζ. The probability density function of ζ is proportional to $1 - \zeta$ for $\zeta \in [0,1]$ according to the algorithm. Subsequently, sample a set of random numbers $\{\eta^{(k)}, k = 1, \ldots, F \text{ and } k \neq j_{\text{occ}}\}$ from a uniform distribution on domain $[0, 1-\zeta]$. The initial value of action variables is assigned as

$$e_0^{(k)} = \begin{cases} 1+\zeta, & \text{if } k = j_{\text{occ}} \\ \eta^{(k)}, & \text{otherwise} \end{cases} . \tag{S23}$$

The initial value of each angle variable, $\theta_0^{(k)}$ $(k = 1, \ldots, F)$, is independently sampled from a uniform distribution on domain $[0, 2\pi)$.

Step 3: The initial value of coordinate-momentum variables for electronic DOFs is obtained from that of action-angle variables by the transformation

$$x_0^{(k)} = \sqrt{2e_0^{(k)}} \cos \theta_0^{(k)}$$
$$p_0^{(k)} = \sqrt{2e_0^{(k)}} \sin \theta_0^{(k)}$$ (S24)

Similarly, in the adiabatic representation, we generate the initial value of action-angle variables $\left(\tilde{\mathbf{e}}_0, \tilde{\boldsymbol{\theta}}_0\right)$ from Step 2 and subsequently obtain $\left(\tilde{\mathbf{x}}_0, \tilde{\mathbf{p}}_0\right)$ by Step 3.

3) Initial Value of Commutator Matrix Variables $\boldsymbol{\Gamma}_0$ or $\tilde{\boldsymbol{\Gamma}}_0$ for Electronic DOFs in NaF, NaF-TW, or SQC-TW

NaF-TW, NaF, and SQC-TW differ in the treatment of the initial condition of commutator matrix $\boldsymbol{\Gamma}_0$ in the diabatic representation (or $\tilde{\boldsymbol{\Gamma}}_0$ in the adiabatic representation). When we use NaF-TW in the main text, $\boldsymbol{\Gamma}_0$ (or $\tilde{\boldsymbol{\Gamma}}_0$) is set to the constant matrix $\gamma \mathbf{I}$. As comparison, when we employ NaF or SQC-TW, the initial commutator matrix is expressed as

$$\Gamma_0^{(nm)} = \left(\frac{1}{2}\left(\left(x_0^{(n)}\right)^2 + \left(p_0^{(n)}\right)^2 \right) - \delta_{n, j_{\mathrm{occ}}} \right) \delta_{nm}$$ (S25)

in the diabatic representation, or

$$\tilde{\Gamma}_0^{(nm)} = \left(\frac{1}{2}\left(\left(\tilde{x}_0^{(n)}\right)^2 + \left(\tilde{p}_0^{(n)}\right)^2 \right) - \delta_{n, j_{\mathrm{occ}}} \right) \delta_{nm}$$ (S26)

in the adiabatic representation.

As mentioned in the main text, when the initial condition is defined and the initial sampling is prepared in the diabatic representation, electronic phase space variables $\left(\mathbf{x}_0, \mathbf{p}_0\right)$ as well as commutator matrix $\boldsymbol{\Gamma}_0$ are transformed to their counterparts in the adiabatic representation before performing NaF dynamics.

S2-B: Numerical Integrators for the Equations of Motion for Trajectories

1) Numerical Integrator for NaF-TW or NaF

There are six steps of the numerical integrator for one time interval Δt for updating nuclear coordinate $\mathbf{R}$, nuclear kinematic momentum $\mathbf{P}$, electronic phase variables $\tilde{\mathbf{g}} = \tilde{\mathbf{x}} + i\tilde{\mathbf{p}}$, and commutator matrix $\tilde{\Gamma}$ in the adiabatic representation. As first discussed in ref[3], nuclear kinematic momentum $\mathbf{P}$ in the adiabatic representation is equivalent to the mapping nuclear momentum in the diabatic representation.

Step 1: Propagate the nuclear kinematic momentum within half a time step $\Delta t/2$

$$\mathbf{P}_{t+\Delta t/2} \leftarrow \mathbf{P}_t + \left(-\nabla_{\mathbf{R}} E_{j_{\mathrm{occ}}(t)}(\mathbf{R}_t) + \mathbf{f}_{\mathrm{nonadia}}(t) \right) \frac{\Delta t}{2}, \tag{S27}$$

where $-\nabla_{\mathbf{R}} E_{j_{\mathrm{occ}}}(\mathbf{R}_t)$ represents the state-specific adiabatic nuclear force evolving on the $j_{\mathrm{occ}}(t)$-th adiabatic state, and $\mathbf{f}_{\mathrm{nonadia}}(t) = -\sum_{k \neq l} \left[\left(E_k(\mathbf{R}_t) - E_l(\mathbf{R}_t) \right) \mathbf{d}_{lk}(\mathbf{R}_t) \right] \tilde{\rho}_{kl}(t)$ stands for the nonadiabatic nuclear force. Here, $\tilde{\rho}(t)$ denotes the electronic quasi-density matrix, which is

$$\tilde{\rho}(t) = \frac{1}{2} \tilde{\mathbf{g}}_t \tilde{\mathbf{g}}_t^\dagger - \tilde{\Gamma}_t \tag{S28}$$

for NaF, or

$$\tilde{\rho}(t) = \left(1 + F/3 \right) \tilde{\mathbf{g}}_t \tilde{\mathbf{g}}_t^\dagger / \mathrm{Tr}_e \left[\tilde{\mathbf{g}}_t \tilde{\mathbf{g}}_t^\dagger \right] - 1/3 \tag{S29}$$

for NaF-TW.

Step 2: Propagate the nuclear coordinate within a full time step Δt

$$\mathbf{R}_{t+\Delta t} \leftarrow \mathbf{R}_t + \mathbf{M}^{-1} \mathbf{P}_{t+\Delta t/2} \Delta t. \tag{S30}$$

Step 3: Propagate electronic phase variables within a full time step Δt according to

$$\tilde{\mathbf{g}}_{t+\Delta t} \leftarrow \tilde{\mathbf{U}}(\mathbf{R}_{t+\Delta t}, \mathbf{P}_{t+\Delta t/2}; \Delta t)\tilde{\mathbf{g}}_t .\tag{S31}$$

Here, $\tilde{\mathbf{U}}(\mathbf{R}_t, \mathbf{P}_t; \Delta t) = \exp\left[-i\Delta t \mathbf{V}^{(\mathrm{eff})}(\mathbf{R}_t, \mathbf{P}_t)\right]$ denotes the unitary short-time propagator within a full time step Δt in the adiabatic representation. Moreover, in the case of NaF, the EOM for commutator matrix $\tilde{\boldsymbol{\Gamma}}$ reads $\dot{\tilde{\boldsymbol{\Gamma}}} = i\left[\tilde{\boldsymbol{\Gamma}} \mathbf{V}^{(\mathrm{eff})}(\mathbf{R}, \mathbf{P}) - \mathbf{V}^{(\mathrm{eff})}(\mathbf{R}, \mathbf{P})\tilde{\boldsymbol{\Gamma}}\right]$, leading to the propagator within a full time step Δt,

$$\tilde{\boldsymbol{\Gamma}}_{t+\Delta t} \leftarrow \tilde{\mathbf{U}}(\mathbf{R}_{t+\Delta t}, \mathbf{P}_{t+\Delta t/2}; \Delta t)\tilde{\boldsymbol{\Gamma}}_t \tilde{\mathbf{U}}^\dagger(\mathbf{R}_{t+\Delta t}, \mathbf{P}_{t+\Delta t/2}; \Delta t) .\tag{S32}$$

When it is more convenient to utilize potential energy surfaces in the diabatic representation, the short-time propagator in the adiabatic representation can be replaced with $\mathbf{T}^\dagger(\mathbf{R}_{t+\Delta t})\exp\left[-i\Delta t \mathbf{V}(\mathbf{R}_{t+\Delta t})\right]\mathbf{T}(\mathbf{R}_t)$, where $\mathbf{T}(\mathbf{R})$ represents the diabatic-to-adiabatic transformation matrix with elements $T_{nm}(\mathbf{R}) = \langle n | \phi_m(\mathbf{R}) \rangle$ and $\mathbf{V}(\mathbf{R})$ denotes the diabatic potential energy matrix.

Step 4: Update $j_{\mathrm{occ}}(t)$ to a new occupied state $j_{\mathrm{occ}}(t + \Delta t)$ based on the switching strategy, i.e., select the state with the largest weight. We then rescale nuclear kinematic momentum $\mathbf{P}$ if $j_{\mathrm{occ}}(t + \Delta t) \neq j_{\mathrm{occ}}(t)$,

$$\mathbf{P}_{t+\Delta t/2} \leftarrow \mathbf{P}_{t+\Delta t/2}\sqrt{\frac{H_{\mathrm{NaF}}(\mathbf{R}_{t+\Delta t}, \mathbf{P}_{t+\Delta t/2}, \tilde{\mathbf{x}}_{t+\Delta t}, \tilde{\mathbf{p}}_{t+\Delta t}) - E_{j_{\mathrm{occ}}(t+\Delta t)}(\mathbf{R}_{t+\Delta t})}{\mathbf{P}_{t+\Delta t/2}^T \mathbf{M}^{-1}\mathbf{P}_{t+\Delta t/2}/2}} .\tag{S33}$$

If $H_{\mathrm{NaF}}(\mathbf{R}_{t+\Delta t}, \mathbf{P}_{t+\Delta t/2}, \tilde{\mathbf{x}}_{t+\Delta t}, \tilde{\mathbf{p}}_{t+\Delta t}) < E_{j_{\mathrm{occ}}(t+\Delta t)}(\mathbf{R}_{t+\Delta t})$, the switching of the adiabatic nuclear force component is frustrated. In such a case we keep $j_{\mathrm{occ}}(t + \Delta t) = j_{\mathrm{occ}}(t)$ and the rescaling step of eq (S33) is skipped.

Step 5: Propagate the nuclear kinematic momentum within the other half time step $\Delta t/2$

$$\mathbf{P}_{t+\Delta t} \leftarrow \mathbf{P}_{t+\Delta t/2} + \left(-\nabla_{\mathbf{R}} E_{j_{occ}(t+\Delta t)}(\mathbf{R}_{t+\Delta t}) + \mathbf{f}_{nonadia}(t+\Delta t)\right)\frac{\Delta t}{2}. \tag{S34}$$

Step 6: Finally, rescale the nuclear kinematic momentum $\mathbf{P}$ again to ensure energy conservation in the mapping variables:

$$\mathbf{P}_{t+\Delta t} \leftarrow \mathbf{P}_{t+\Delta t}\sqrt{\frac{H_{NaF}(\mathbf{R}_0,\mathbf{P}_0,\tilde{\mathbf{x}}_0,\tilde{\mathbf{p}}_0) - E_{j_{occ}(t+\Delta t)}(\mathbf{R}_{t+\Delta t})}{\mathbf{P}_{t+\Delta t}^T \mathbf{M}^{-1}\mathbf{P}_{t+\Delta t}/2}}. \tag{S35}$$

If $H_{NaF}(\mathbf{R}_0,\mathbf{P}_0,\tilde{\mathbf{x}}_0,\tilde{\mathbf{p}}_0) < E_{j_{occ}(t+\Delta t)}(\mathbf{R}_{t+\Delta t})$, i.e., the total mapping energy on phase space is smaller than the pure adiabatic potential energy, it indicates that the time step size Δt is relatively large for the integrator from time t to time $t+\Delta t$. In such a case, one should then choose a smaller time step size Δt and repeat Steps 1-6 for the update of $(\mathbf{R}_{t+\Delta t},\mathbf{P}_{t+\Delta t},\tilde{\mathbf{x}}_{t+\Delta t},\tilde{\mathbf{p}}_{t+\Delta t})$ from $(\mathbf{R}_t,\mathbf{P}_t,\tilde{\mathbf{x}}_t,\tilde{\mathbf{p}}_t)$. The time step size Δt should be adjusted in the region where the sum of adiabatic and nonadiabatic nuclear force terms is relatively large.

The rescaling of $\mathbf{P}$ along its direction is used in the numerical propagator in order to ensure the energy conservation. Alternatively, in Steps 1 and 5, $\mathbf{f}_{nonadia}$ of eq (S27) and eq (S34) can also be replaced by its projected component $\mathbf{f}_{nonadia}^{\perp}$ perpendicular to the velocity vector, $\dot{\mathbf{R}} = \mathbf{M}^{-1}\mathbf{P}$. That is,

$$\mathbf{f}_{nonadia}^{\perp} = \mathbf{f}_{nonadia} - \frac{\mathbf{f}_{nonadia}\cdot\dot{\mathbf{R}}}{\dot{\mathbf{R}}\cdot\dot{\mathbf{R}}}\dot{\mathbf{R}}. \tag{S36}$$

2) Numerical Integrator for SQC-TW or Ehrenfest Dynamics

In contrast to the aforementioned NaF integrator, both SQC-TW and Ehrenfest dynamics employ the mean field picture instead of the nonadiabatic field picture. In the mean field picture, the integrator also includes Steps 1, 2, 3, and 5 of the NaF/NaF-TW integrator. The difference is that, in the integrator for the EOMs for trajectories of either SQC-TW or Ehrenfest dynamics, the full nuclear force (i.e., the time derivative of $\mathbf{P}$) in Step 1 and Step 5 is defined by

$$\dot{\mathbf{P}} = \mathbf{f}_{mf}(t) = -\sum_{k,l} \left[\nabla_{\mathbf{R}} E_k(\mathbf{R}_t)\delta_{kl} + (E_k(\mathbf{R}_t) - E_l(\mathbf{R}_t))\mathbf{d}_{lk}(\mathbf{R}_t) \right] \tilde{\rho}_{kl}(t) . \tag{S37}$$

When SQC-TW is used, $\tilde{\rho}(t) = \frac{1}{2}\tilde{\mathbf{g}}_t\tilde{\mathbf{g}}_t^\dagger - \tilde{\mathbf{\Gamma}}_0$, where commutator matrix $\tilde{\mathbf{\Gamma}}$ does *not* evolve with time. This corresponds to the "trajectory-adjusted zero-point energy" treatment of the SQC approach with triangle window functions of Cotton and Miller in ref[4]. (We note that, in the SQC-TW approach, only the expression of the electronic population-population correlation function is the same as that of ref[4], while those of the other three kinds of time correlation functions for electronic DOFs are not from ref[4] but constructed in the main text of the present letter.)

When Ehrenfest dynamics is employed, we have $\tilde{\rho}(t) = \frac{1}{2}\tilde{\mathbf{g}}_t\tilde{\mathbf{g}}_t^\dagger$ instead.

3) Numerical Integrator for FSSH

FSSH employs the adiabatic nuclear force picture rather than the nonadiabatic field picture. In the FSSH algorithm[5, 6], the full nuclear force in Step 1 and Step 5 (of the numerical integrator of NaF/NaF-TW) is $\dot{\mathbf{P}} = \mathbf{f}_{adia}(t) = -\nabla_{\mathbf{R}} E_{j_{occ}(t)}(\mathbf{R}_t)$ instead, and Step 4 (of the numerical integrator of NaF/NaF-TW) is replaced with the FSSH strategy (i.e., eq (S51) of the Supporting Information of ref[7]) to determine a new occupied state $j_{occ}(t + \Delta t)$. The detailed description of the numerical integrator for FSSH is described in Section S7 of the Supporting Information of ref[7].

S2-C: Numerical Evaluation of the Time Correlation Function for NaF, NaF-TW and SQC-TW

1) Evaluation of the Time Correlation Function for NaF

The sampling of the initial condition of phase space variables of NaF, as described by the instruction in Sub-section S2-A, is performed multiple times for generating a collection of N_{samp} numbers of initial conditions for trajectories, i.e., $\left\{\left(\mathbf{x}_{0;[s]}, \mathbf{p}_{0;[s]}, \mathbf{\Gamma}_{0;[s]}, \mathbf{R}_{0;[s]}, \mathbf{P}_{0;[s]}\right), \ s = 1, \ldots, N_{samp}\right\}$. Each initial condition is then used for evolving a trajectory by the numerical integrator of NaF described in Sub-section S2-B, i.e., $\left(\mathbf{x}_{0;[s]}, \mathbf{p}_{0;[s]}, \mathbf{\Gamma}_{0;[s]}, \mathbf{R}_{0;[s]}, \mathbf{P}_{0;[s]}\right)$ evolves to $\left(\mathbf{x}_{t;[s]}, \mathbf{p}_{t;[s]}, \mathbf{\Gamma}_{t;[s]}, \mathbf{R}_{t;[s]}, \mathbf{P}_{t;[s]}\right)$ at time t. The time correlation function is evaluated by the following summation,

$$
\mathrm{Tr}_{n,e}\left[\left(|n\rangle\langle m|\otimes\hat{\rho}_{\mathrm{nuc}}\right)e^{i\hat{H}t/\hbar}\left(|k\rangle\langle l|\otimes\hat{A}_{\mathrm{nuc}}\right)e^{-i\hat{H}t/\hbar}\right]
$$

$$
\mapsto \frac{1}{N_{samp}}\sum_{s=1}^{N_{samp}}\left[\frac{1}{2}\left(x_{0;[s]}^{(m)}+ip_{0;[s]}^{(m)}\right)\left(x_{0;[s]}^{(n)}-ip_{0;[s]}^{(n)}\right)-\gamma\delta_{mn}\right] \qquad (S38)
$$

$$
\times\left[\frac{1+F}{2\left(1+F\gamma\right)^{2}}\left(x_{t;[s]}^{(l)}+ip_{t;[s]}^{(l)}\right)\left(x_{t;[s]}^{(k)}-ip_{t;[s]}^{(k)}\right)-\frac{1-\gamma}{1+F\gamma}\delta_{lk}\right]A_{W}\left(\mathbf{R}_{t;[s]},\mathbf{P}_{t;[s]}\right)
$$

2) Evaluation of the Time Correlation Function for NaF-TW and SQC-TW

According to the numerical procedures of NaF-TW or those of SQC-TW in Sub-sections S2-A and S2-B, N_{samp} numbers of initial conditions $\left\{\left(\mathbf{x}_{0;[s]}, \mathbf{p}_{0;[s]}, \mathbf{R}_{0;[s]}, \mathbf{P}_{0;[s]}\right), \ s = 1, \ldots, N_{samp}\right\}$ are generated and propagated to $\left\{\left(\mathbf{x}_{t;[s]}, \mathbf{p}_{t;[s]}, \mathbf{R}_{t;[s]}, \mathbf{P}_{t;[s]}\right), \ s = 1, \ldots, N_{samp}\right\}$ for NaF-TW; or similarly, N_{samp} numbers of initial conditions $\left\{\left(\mathbf{x}_{0;[s]}, \mathbf{p}_{0;[s]}, \mathbf{\Gamma}_{0;[s]}, \mathbf{R}_{0;[s]}, \mathbf{P}_{0;[s]}\right), \ s = 1, \ldots, N_{samp}\right\}$ are sampled and evolved to $\left\{\left(\mathbf{x}_{t;[s]}, \mathbf{p}_{t;[s]}, \mathbf{R}_{t;[s]}, \mathbf{P}_{t;[s]}\right), \ s = 1, \ldots, N_{samp}\right\}$ for time t for SQC-TW. The population-

population ($n = m$ and $k = l$) or population-coherence ($n = m$ and $k \neq l$) correlation function is

evaluated by the following summation over trajectories,

$$
\mathrm{Tr}_{n,e}\left[\left(|n\rangle\langle n|\otimes \hat{\rho}_{\mathrm{nuc}}\right)e^{i\hat{H}t/\hbar}\left(|k\rangle\langle l|\otimes \hat{A}_{\mathrm{nuc}}\right)e^{-i\hat{H}t/\hbar}\right]
$$

$$
\mapsto \begin{cases} \dfrac{\displaystyle\sum_{s=1}^{N_{\mathrm{samp}}} K_{kk}^{\mathrm{bin}}\left(\mathbf{x}_{t;[s]},\mathbf{p}_{t;[s]}\right)A_{W}\left(\mathbf{R}_{t;[s]},\mathbf{P}_{t;[s]}\right)}{\displaystyle\sum_{s=1}^{N_{\mathrm{samp}}}\sum_{i=1}^{F} K_{ii}^{\mathrm{bin}}\left(\mathbf{x}_{t;[s]},\mathbf{p}_{t;[s]}\right)}, \quad \text{for } k = l \\[2em] \dfrac{1}{N_{\mathrm{samp}}}\displaystyle\sum_{s=1}^{N_{\mathrm{samp}}} K_{kl}^{\mathrm{CMM}}\left(\mathbf{x}_{t;[s]},\mathbf{p}_{t;[s]}\right)A_{W}\left(\mathbf{R}_{t;[s]},\mathbf{P}_{t;[s]}\right), \quad \text{for } k \neq l \end{cases}, \qquad \text{(S39)}
$$

where $K_{kk}^{\mathrm{bin}}\left(\mathbf{x},\mathbf{p}\right)$ and $K_{kl}^{\mathrm{CMM}}\left(\mathbf{x},\mathbf{p}\right)$ are defined as eqs (16) and (19) of the main text (of the present

letter). The coherence-population ($n \neq m$ and $k = l$) or coherence-coherence ($n \neq m$ and $k \neq l$)

correlation function is estimated by

$$
\mathrm{Tr}_{n,e}\left[\left(|n\rangle\langle m|\otimes \hat{\rho}_{\mathrm{nuc}}\right)e^{i\hat{H}t/\hbar}\left(|k\rangle\langle l|\otimes \hat{A}_{\mathrm{nuc}}\right)e^{-i\hat{H}t/\hbar}\right]
$$

$$
\mapsto \frac{12}{5N_{\mathrm{samp}}}\sum_{s=1}^{N_{\mathrm{samp}}} K_{mn}^{\mathrm{CMM}}\left(\mathbf{x}_{0;[s]},\mathbf{p}_{0;[s]}\right)K_{lk}^{\mathrm{CMM}}\left(\mathbf{x}_{t;[s]},\mathbf{p}_{t;[s]}\right)A_{W}\left(\mathbf{R}_{t;[s]},\mathbf{P}_{t;[s]}\right). \qquad \text{(S40)}
$$

S3: Simulation Details for Models

S3-A: Reduced Electronic Dynamics for System-Bath Models.

For system-bath models, the system is always bilinearly coupled with harmonic bath DOFs of a

dissipative environment in the condensed phase. The system-bath coupling, representing the

substantial influence from the bath environment, governs the dynamics of the system across a

spectrum ranging from coherent to dissipative regimes. These models serve as pivotal tools for

understanding electron/exciton dynamics in chemical and biological reactions. Numerically exact

results of the spin-boson model can be achieved by quasi-adiabatic propagator path integral

(QuAPI)[8-10] and more efficient small matrix PI (SMatPI)[11, 12], hierarchy equations of motion

(HEOM)[13-17], (multi-layer) multi-configuration time-dependent Hartree [(ML-)MCTDH] [18-20], and time-dependent density matrix renormalization group (TD-DMRG)[21].

In the present paper, we test two distinctive models: the two-site spin-boson models and the seven-site Fenna–Matthews–Olson (FMO) Monomer model.

Spin-Boson Model: The two-site spin-boson models stand as a fundamental prototype for comprehension of electron transfer and energy transport phenomena. The Hamiltonian for spin-boson models reads $\hat{H} = \hat{H}_B + \hat{H}_{SB} + \hat{H}_S$ with employing the environment bath part $\hat{H}_B$, the linear coupling term $\hat{H}_{S-B}$ and the system part $\hat{H}_S$ as

$$\hat{H}_B = \sum_{j=1}^{N_b} \frac{1}{2}\left(\hat{P}_j^2 + \omega_j^2 \hat{R}_j^2\right)$$

$$\hat{H}_{SB} = \sum_{j=1}^{N_b} c_j \hat{R}_j \left(|1\rangle\langle 1| - |2\rangle\langle 2|\right) \quad \text{(S41)}$$

$$\hat{H}_S = \varepsilon\left(|1\rangle\langle 1| - |2\rangle\langle 2|\right) + \Delta\left(|1\rangle\langle 2| + |2\rangle\langle 1|\right)$$

Here ε denotes the energy bias while Δ signifies the tunneling between states $|1\rangle$ and $|2\rangle$. The bath is discretized into a series of quantum harmonic oscillators, with $\{\hat{P}_j\}$, $\{\hat{R}_j\}$, $\{\omega_j\}$ and $\{c_j\}$ representing the mass-weighted momentum, coordinate, frequencies and the coupling coefficients of the *j*-th oscillator, respectively. For spin-boson models, we adopt the discretization scheme proposed in refs [22, 23] for the Ohmic spectral density $J(\omega) = \frac{\pi}{2}\alpha\omega\exp\left(-\omega/\omega_c\right)$ with the Kondo parameter α and the cut-off frequency ω_c, as depicted below:

$$\begin{cases} \omega_j = -\omega_c \ln\left(1 - \frac{j}{1+N_b}\right) \\ c_j = \omega_j \sqrt{\frac{\alpha\omega_c}{N_b+1}} \end{cases}, \quad j = 1,\cdots,N_b. \quad \text{(S42)}$$

In our simulation, we investigate four specific spin-boson models outlined in ref [24]. These models span a range of system-bath coupling strengths from weak to strong (small to large α), and the cut-off frequency ω_c from low to high. In addition, all simulations are performed at low temperatures ($\beta = 5$) and utilize three hundred discrete bath modes to characterize the Ohmic spectral density within the spin-boson models.

FMO Monomer Model: The FMO complex derived from green sulfur bacteria serves as a prototype system crucial for investigating photosynthetic organisms[25-32]. Specifically referencing ref [29], the FMO monomer employs a site-exciton model, encompassing a seven-site structure coupled with a harmonic bath, whose three parts of Hamiltonian alternatively reads,

$$\hat{H}_B = \sum_{n=1}^{F} \sum_{j=1}^{N_b} \left(\hat{P}_{nj}^2 + \omega_j^2 \hat{R}_{nj}^2 \right) / 2$$

$$\hat{H}_{SB} = \sum_{n=1}^{F} \sum_{j=1}^{N_b} c_j \hat{R}_{nj} |n\rangle\langle n|$$

$$\hat{H}_S = \sum_{n,m=1}^{F} H_{S,nm} |n\rangle\langle m|$$

$$= \begin{pmatrix} 12410 & -87.7 & 5.5 & -5.9 & 6.7 & -13.7 & -9.9 \\ -87.7 & 12530 & 30.8 & 8.2 & 0.7 & 11.8 & 4.3 \\ 5.5 & 30.8 & 12210 & -53.5 & -2.2 & -9.6 & 6.0 \\ -5.9 & 8.2 & -53.5 & 12320 & -70.7 & -17.0 & -63.3 \\ 6.7 & 0.7 & -2.2 & -70.7 & 12480 & 81.1 & -1.3 \\ -13.7 & 11.8 & -9.6 & -17.0 & 81.1 & 12630 & 39.7 \\ -9.9 & 4.3 & 6.0 & -63.3 & -1.3 & 39.7 & 12440 \end{pmatrix} \text{cm}^{-1} \quad \text{(S43)}$$

Here the variables $\left\{ \hat{P}_{nj}, \hat{R}_{nj} \right\}$ denote the mass-weighted momentum and coordinate of the *j*-th quantum harmonic oscillator for the bath on *n*-th site, and the bath frequencies $\left\{ \omega_j \right\}$ and system-bath coupling coefficients $\left\{ c_j \right\}$ are determined by discretizing the spectral density. Specifically, we utilize the Debye spectral density $J(\omega) = 2\lambda\omega_c\omega / \left(\omega^2 + \omega_c^2 \right)$ for each site, with parameters

$\lambda = 35 \text{ cm}^{-1}$ for the bath reorganization energy and $\omega_c = 106.14 \text{ cm}^{-1}$ for the characteristic frequency. We use the discretization scheme of refs [19, 33, 34],

$$\omega_j = \omega_c \tan\left(\frac{\pi}{2} - \frac{\pi j}{2(N_b + 1)}\right), \quad j = 1, \cdots, N_b$$
$$c_j = \omega_j \sqrt{\frac{2\lambda}{N_b + 1}}, \quad j = 1, \cdots, N_b \tag{S44}$$

for the Debye spectral density. (In comparison, eq (S42) is the discretization scheme for the Ohmic spectral density by following refs [22, 23].) A challenging temperature $T = 77\text{K}$ is investigated as studied in our previous work[35]. The first site of the system is initially occupied, and the bath DOFs are sampled from the Wigner distributions of the corresponding harmonic oscillators. In the FMO monomer model, one hundred discrete bath modes per site (totaling $N_b = 100$) are used to represent the continuous Debye spectral density.

We consider the decoupled initial condition for both spin-boson models and the FMO monomer model, where the system is in the excited state and the bath modes are at the thermal equilibrium (i.e., the quantum Boltzmann distribution for the pure bath Hamiltonian operator). Specially, the bath modes are sampled from the corresponding Wigner distribution

$$\rho_W(\mathbf{R}, \mathbf{P}) \propto \exp\left[-\sum_{j=1}^{N_b} \frac{\beta}{2Q(\omega_j)}(P_j^2 + \omega_j^2 R_j^2)\right] \tag{S45}$$

with $Q(\omega) = \dfrac{\beta\hbar\omega/2}{\tanh(\beta\hbar\omega/2)}$ as the quantum corrector[36]. For both the spin-boson models and the FMO monomer model, we use the exact results obtained from our previous work[24] using HEOM/extended HEOM (eHEOM)[37, 38] for comparison.
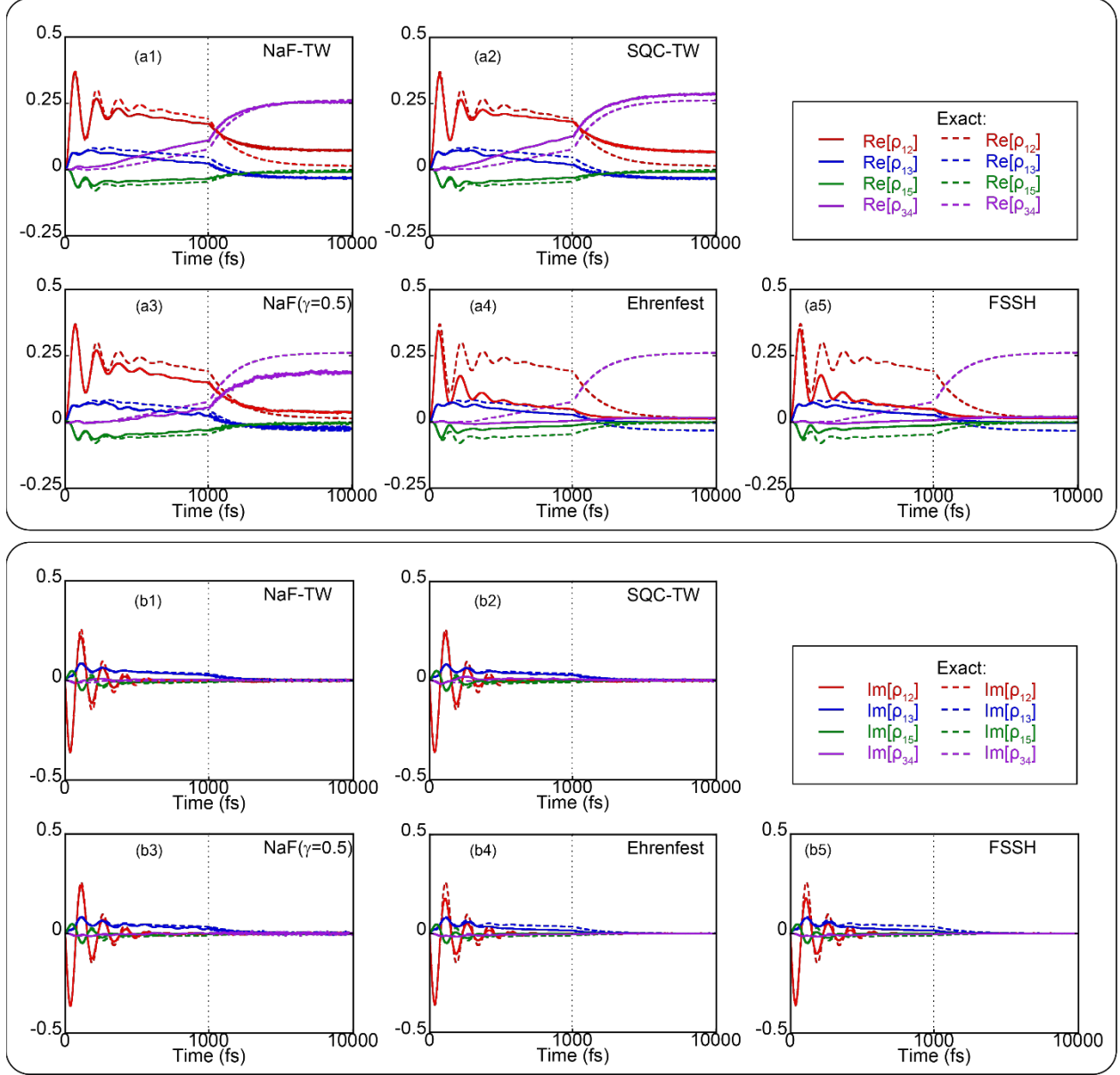
Figure S1. Dynamics of the off-diagonal (coherence) terms of the reduced electronic density matrix of the seven-site FMO monomer model at temperature 77 K. The real part and imaginary parts are presented in panel (a) and panel (b), respectively. Panel (a): The red, blue, green, and purple solid lines illustrate the real part of $\rho_{12}(t)$, $\rho_{13}(t)$, $\rho_{15}(t)$ and $\rho_{34}(t)$, respectively. Panel (b): Similar to panel (a), but the red, blue, green, and purple solid lines depict the imaginary part of $\rho_{12}(t)$, $\rho_{13}(t)$, $\rho_{15}(t)$ and $\rho_{34}(t)$, respectively. The exact results produced by HEOM are

presented by dashed lines in corresponding colors. Sub-panels (a1-a5) or sub-panels (b1-b5) denote the results of NaF-TW, SQC-TW, NaF($\gamma = 0.5$), Ehrenfest dynamics, and FSSH, respectively. One hundred discrete bath modes for each site are employed to obtain converged results.

S3-B: Cavity Quantum Electrodynamic for Atom-in-Cavity Models.

It has been observed that several significant phenomena manifest in cavity quantum electrodynamics (cQED), particularly under conditions where matter is tightly coupled to the vacuum field within a confined optical cavity[39-42]. In the main text, we examine benchmark cQED models featuring a multi-level hydrogen atom confined within a one-dimensional lossless cavity[43-46]. The atomic system is coupled to multi-cavity-modes, whose Hamiltonian is described by F atomic energy levels:

$$\hat{H} = \sum_{n=1}^{F} \varepsilon_n |n\rangle\langle n| + \sum_{j=1}^{N} \frac{1}{2}\left(\hat{P}_j^2 + \omega_j^2 \hat{R}_j^2\right) + \sum_{j=1}^{N} \omega_j \lambda_j (r_0) \hat{R}_j \sum_{n \neq m}^{F} \mu_{nm} |n\rangle\langle m|, \qquad (S46)$$

where ε_n is the atomic energy level of the n-th atomic state, and we employ a three-state model with the energy levels $\varepsilon_1 = -0.6738$, $\varepsilon_2 = -0.2798$, $\varepsilon_3 = -0.1547$, and μ_{nm} denotes the transitional dipole moment with nonzero values $\mu_{12} = -1.034$, $\mu_{23} = -2.536$ (all in atomic units). The first model involves full three atomic levels, and the second one is a reduced two-level model where only the two lowest levels are considered. The variables, $\hat{R}_j, \hat{P}_j, \omega_j$ denote the canonical coordinate, canonical momentum, and frequency of the j -th optical field mode, respectively, and the atom-optical field interaction reads

$$\lambda_j (r_0) = \sqrt{\frac{2}{\varepsilon_0 L}} \sin\left(\frac{j\pi r_0}{L}\right), \quad j = 1, \cdots, N , \qquad (S47)$$

where L, ε_0 and r_0 denote the volume length of cavity, the vacuum permittivity, and the location of the atom, respectively. We fix $L = 236200$ a.u. and $r_0 = L/2$, and employ four hundred standing-wave modes for the optical field, with the frequency ω_j of the j-th mode set to $j\pi c / L$ (Here $c = 137.036$ a.u. denotes the light speed in vacuum). Initially, the highest atomic level is excited, while all cavity modes remain in the vacuum state. Subsequently, spontaneous emission occurs, releasing a photon that traverses the cavity and reflects back to interact with the atom. The re-absorption and re-emission processes then follow. We compare our results with benchmark data obtained from truncated configuration interaction calculations, as reported in refs [43, 44].

S3-C: Dynamics around Conical Intersection for Linear Vibronic Coupling Models.

The linear vibronic coupling model (LVCM) is a straightforward yet powerful model that simulates molecular systems, particularly those where the conical intersection (CI) region is pivotal, such as in light-induced processes. In the diabatic representation, the Hamiltonian of LVCM is expressed as

$$\hat{H} = \sum_{k=1}^{N} \frac{\omega_k}{2} \left(\hat{P}_k^2 + \hat{R}_k^2 \right) + \sum_{n=1}^{F} \left(E_n + \sum_{k=1}^{N} \kappa_k^{(n)} \hat{R}_k \right) |n\rangle\langle n| + \sum_{n \neq m}^{F} \left(\sum_{k=1}^{N} \lambda_k^{(nm)} \hat{R}_k \right) |n\rangle\langle m|, \qquad (S48)$$

where E_n $(n = 1,...,F)$ is the vertical excitation energy of the n-th state, while $\hat{P}_k$ and $\hat{R}_k$ $(k = 1,...,N)$ denote dimensionless weighted normal-mode momentum and coordinate of the k-th nuclear DOF, respectively, with the corresponding frequency ω_k. In addition, parameters $\kappa_k^{(n)}$ and $\lambda_k^{(nm)}$ represent the linear coupling coefficients of the k-th nuclear vibronic DOF with the diagonal and off-diagonal elements of the electronic density, respectively.

In our first case study, we explore two versions of the linear vibronic coupling model (LVCM) applied to the S1/S2 conical intersection of the pyrazine molecule. One LVCM variant includes three nuclear modes, while the other incorporates 24 nuclear modes. Detailed parameters for these models can be found in refs [47, 48]. The initial state consists of the cross-product between the vibronic ground state and the electronically excited diabatic state (S2). Furthermore, we investigate a typical three-electronic-state LVCM with two nuclear modes for the $Cr(CO)_5$ molecule, as detailed in ref [49]. Here, the initial condition comprises the cross-product of the first electronically excited diabatic state and a Gaussian nuclear wave-packet. The Gaussian wave-packet is centered at the minimum point of the ground state of the $Cr(CO)_6$ molecule, where a carbonyl group dissociates. The width of each mode is determined by the corresponding vibrational frequencies. While we employ the diabatic representation for initializing and evaluating dynamical properties, consistent with the approach in MCTDH, we switch to the adiabatic representation for real-time dynamics to ensure fair comparison among different non-adiabatic dynamics methods. The parameter lists for the LVCMs applied to both the pyrazine and $Cr(CO)_5$ molecules can be found in the Supporting Information, specifically in Tables S2-S4 of ref [7].

S3-D: Photodissociation Dynamics of Gas Phase Models with One Nuclear Degree of Freedom.

We further test gas phase models with asymptotic regions. We consider the coupled three-electronic-state photodissociation models of Miller and coworkers [50]. Each PES is described by a Morse oscillator and the coupling terms are depicted by Gaussian functions:

$$
\begin{aligned}
V_{ii}(R) &= D_i \left[1 - e^{-\beta_i(R-R_i)} \right]^2 + C_i, \quad i = 1,2,3. \\
V_{ij}(R) &= V_{ji}(R) = A_{ij} e^{-\alpha_{ij}(R-R_{ij})^2}, \quad i,j = 1,2,3; \text{ and } i \neq j.
\end{aligned}
\tag{S49}
$$

where the detailed parameters match those of Model III as described in ref [50]. The Wigner distribution for nuclear DOF is $\rho_W(R,P) \propto \exp\left(-m\omega(R-R_e)^2 - P^2/m\omega\right)$, where $m = 20000$ a.u. is the mass of the nuclear DOF, $\omega = 0.005$ a.u. is the vibrational frequency of ground state, and R_e denotes the center of wavepacket. The first electronic diabatic state is initially occupied. Numerically exact results for the models can be obtained by the discrete variable representation (DVR) approach of ref [51].

S3-E: Nonadiabatic Scattering Dynamics of Tully's Models.

We investigate Tully's three models[6] for nonadiabatic scattering dynamics, namely, the single avoided crossing (SAC) model, the dual avoided crossing (DAC) model and the extended coupling region (ECR) model. The results of the ECR model are demonstrated in the main text. The ECR model poses a formidable challenge for mapping-based methods, involving some trajectories that transmit forward while others reflect—a complex scenario inadequately described within mean-field approximations. The Hamiltonian of ECR model reads

$$
\begin{aligned}
V_{11}(R) &= +E_0 \\
V_{22}(R) &= -E_0 \\
V_{12}(R) &= V_{21}(R) = C\left[e^{BR}h(-R) + (2 - e^{-BR})h(R)\right]
\end{aligned}
\qquad , \qquad (S50)
$$

where $B = 0.9$, $C = 0.1$, $E_0 = -0.0006$, and $h(R)$ represents the Heaviside function. Initially, the system with mass $m = 2000$ a.u. occupies in the electronic adiabatic ground state, and the nuclear wavefunction $\psi(R) \propto e^{-\alpha(R-R_0)^2/2 + iP_0(R-R_0)}$ leads to the corresponding Wigner distribution $\rho_W(R,P) \propto e^{-\alpha(R-R_0)^2 + (P-P_0)^2/\alpha}$. The center of the initial wavefunction, denoted by R_0, is positioned at -13, with a width parameter of $\alpha = 1$. The initial momentum is set to P_0 varying from 2 to 50.

In addition, we also provide supplemental results of trajectory-based dynamics for the SAC model and the DAC model[6]. The SAC model reads

$$V_{11}(R) = A(1 - e^{-B|R|})\,\text{sgn}(R)$$
$$V_{22}(R) = -V_{11}(R)$$
$$V_{12}(R) = V_{21}(R) = Ce^{-DR^2}$$

(S51)

with $A = 0.01$, $B = 1.6$, $C = 0.005$, $D = 1.0$, and initial $R_0 = -3.8$; and the DAC model reads

$$V_{11}(R) = 0$$
$$V_{22}(R) = -Ae^{-BR^2} + E_0$$
$$V_{12}(R) = V_{21}(R) = Ce^{-DR^2}$$

(S52)

with $A = 0.1$, $B = 0.28$, $C = 0.015$, $D = 0.06$, $E_0 = 0.05$ and initial $R_0 = -10$. Other parameters keep the same as those used in the ECR model. Figure S2 presents the transmission probabilities of the SAC and the DAC models. For the SAC model, the results of all methods are close to each other. For the DAC model, NaF, SQC-TW and NaF-TW slightly outperform Ehrenfest dynamics and FSSH, especially in the high kinematic energy region where $P_0 > 20$. Figure S3 depicts the nuclear distribution of the SAC and DAC models in the long time limit, when the center of the momentum of the initial nuclear Gaussian wavepacket is $P_0 = 10$ or $P_0 = 20$. NaF-TW, NAF, and FSSH outperform SQC-TW and Ehrenfest dynamics in the description of the nuclear dynamics.
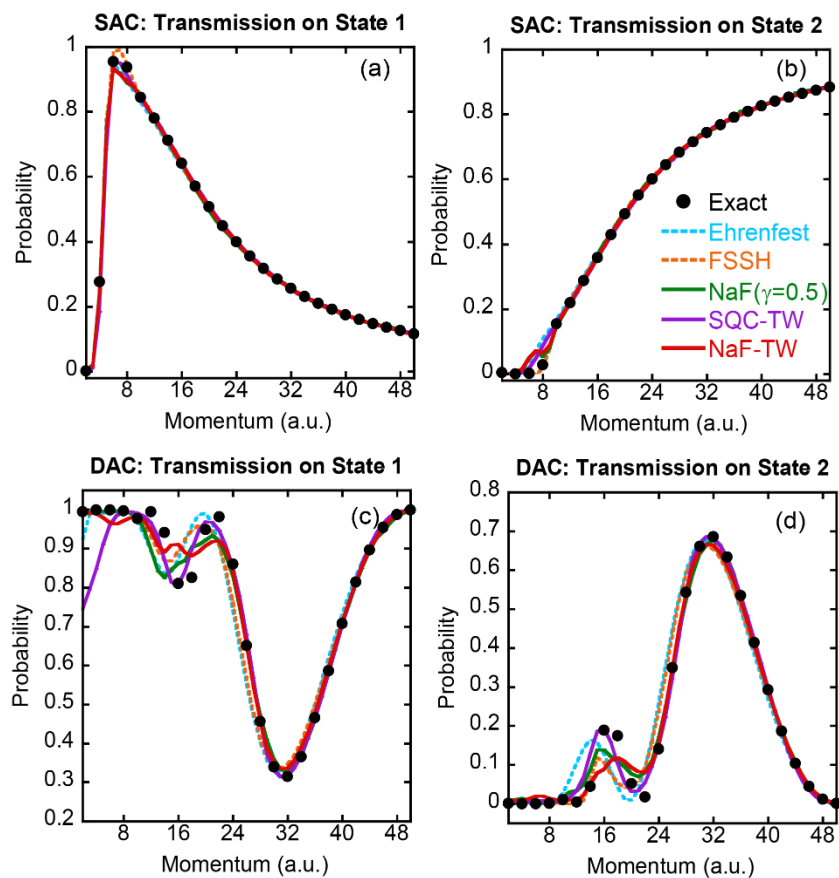
Figure S2. Panels (a-b) describe the transmission probability on (adiabatic) State 1 and that on State 2 for Tully's SAC model. Panels (c-d) present the transmission probability on (adiabatic) State 1 and that on State 2 for Tully's DAC model. Black points: Exact results produced by DVR. Cyan dashed lines: Ehrenfest dynamics. Orange dashed lines: FSSH. Purple solid lines: SQC-TW. Green solid lines: NaF. Red solid lines: NaF-TW.
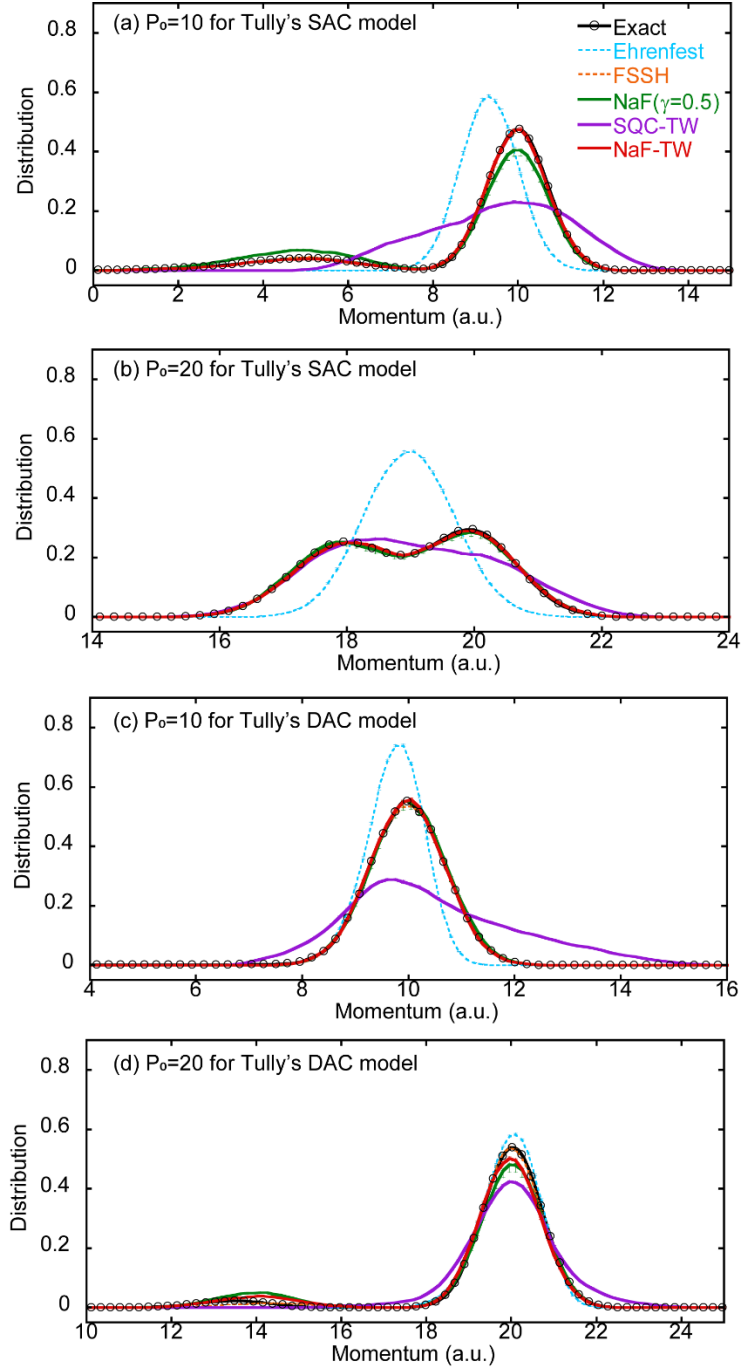
Figure S3. Panels (a-b) describe the asymptotic nuclear momentum distribution for Tully's SAC model, with the initial momentum of the incoming nuclear Gaussian wavepacket centered at $P_0 = 10$ and $P_0 = 20$, respectively. Panels (c-d): same as panels (a-b) but for Tully's DAC model.

Black circles: Exact results produced by DVR. Cyan dashed lines: Ehrenfest dynamics. Purple solid lines: SQC-TW. Green solid lines: NaF. Red solid lines: NaF-TW.

S3-F: Electron Transfer Rate for the Two-Level Model in the Condensed Phase

We apply NaF-TW to calculate the electron transfer rate in the condensed phase. We adopt the model employed in refs [52, 53], which elucidates a two-level system coupled with a solvent bath:

$$\hat{H} = \hat{H}_s\left(\hat{R}_s, \hat{P}_s\right) + \hat{H}_b\left(\mathbf{\hat{R}}, \mathbf{\hat{P}}, \hat{R}_s\right). \tag{S53}$$

Here,

$$
\begin{aligned}
\hat{H}_s\left(\hat{R}_s, \hat{P}_s\right) = \frac{1}{2}\hat{P}_s^2 &+ \left(\frac{1}{2}\varepsilon + \frac{1}{2}\Omega^2\hat{R}_s^2 + c_s\hat{R}_s\right)|1\rangle\langle 1| \\
&+ \left(-\frac{1}{2}\varepsilon + \frac{1}{2}\Omega^2\hat{R}_s^2 - c_s\hat{R}_s\right)|2\rangle\langle 2| \\
&+ \Delta\left(|1\rangle\langle 2| + |2\rangle\langle 1|\right)
\end{aligned}
\tag{S54}
$$

$$\hat{H}_b\left(\mathbf{\hat{R}}, \mathbf{\hat{P}}, \hat{R}_s\right) = \sum_{n=1}^{N_b}\left[\frac{1}{2}\hat{P}_n^2 + \frac{1}{2}\omega_n^2\left(\hat{R}_n + \frac{c_n}{\omega_n^2}\hat{R}_s\right)^2\right], \tag{S55}$$

where $\left\{\hat{P}_s, \hat{R}_s\right\}$ denote the nuclear momentum and coordinate of the reaction DOF, respectively, and $\left\{\hat{P}_n, \hat{R}_n\right\}$ $(n = 1, \cdots, N_b)$ represent those of solvent bath DOFs. The frequencies $\{\omega_n\}$ and the coefficients $\{c_n\}$ $(n = 1, \cdots, N_b)$ for solvent bath are obtained by discretizing the Ohmic spectral density with the Kondo parameter $\alpha = 9.49\times10^{-6}$ and the cut-off frequency $\omega_c = \Omega = 3.5\times10^{-4}$ a.u. The reorganization energy $\lambda = 2.39\times10^{-2}$ a.u., the coupling $\Delta = 5\times10^{-5}$ a.u., and the parameter $c_s = \Omega\sqrt{\lambda/2}$. Parameter ε represents the energy bias. One hundred discrete bath DOFs are utilized in the calculations.

The electron transfer rate is obtained from[54]

$$k = \int_0^\infty dt \, \mathrm{Re} \, C_{FF}(t), \tag{S56}$$

where the flux-flux correlation function is given by

$$C_{FF}(t) = \mathrm{Tr}\left[\hat{\rho}_{\mathrm{nuc}} \hat{F} e^{i\hat{H}t} \hat{F} e^{-i\hat{H}t}\right], \tag{S57}$$

with the flux operator defined as $\hat{F} = i\Delta(|1\rangle\langle 2| - |2\rangle\langle 1|)$. The initial Wigner density distribution

for nuclear DOFs reads

$$\rho_{\mathrm{nuc}}(\mathbf{R}, \mathbf{P}, R_s, P_s) \propto \exp\left[-\sum_{n=1}^{N_b} \frac{\beta\left(P_n^2 + \omega_n^2 R_n^2\right)}{2Q(\omega_n)}\right] \exp\left[-\frac{\beta\left(P_s^2 + \Omega^2 R_s^2 + 2c_s R_s\right)}{2Q(\Omega)}\right], \tag{S58}$$

with the temperature set at 300 K.

In the region of weak coupling and relative high temperature, the Marcus electron transfer rate theory[55] is anticipated to perform reasonably well and is utilized as a reference for comparison. The results of electron transfer rate produced by NaF-TW, NaF ($\gamma = 0.5$), SQC-TW, SQC-TW2 and NaF-TW2 are compared with those predicted by the Marcus theory in Figure S4. (The details of SQC-TW2 and NaF-TW2 are described in Section S4 of this Supporting Information.) We also present the results (from ref [53]) obtained by an earlier version of SQC where square window functions were utilized. Figure S4 depicts the relationship between the electronic transfer rate k and the bias ε. The results obtained from NaF-TW, NaF ($\gamma = 0.5$), SQC-TW, SQC-TW2 and NaF-TW2 exhibit good agreement with the Marcus theory in both the normal and inverted regimes. The three approaches overall outperform the SQC approach with square window functions in ref [53].
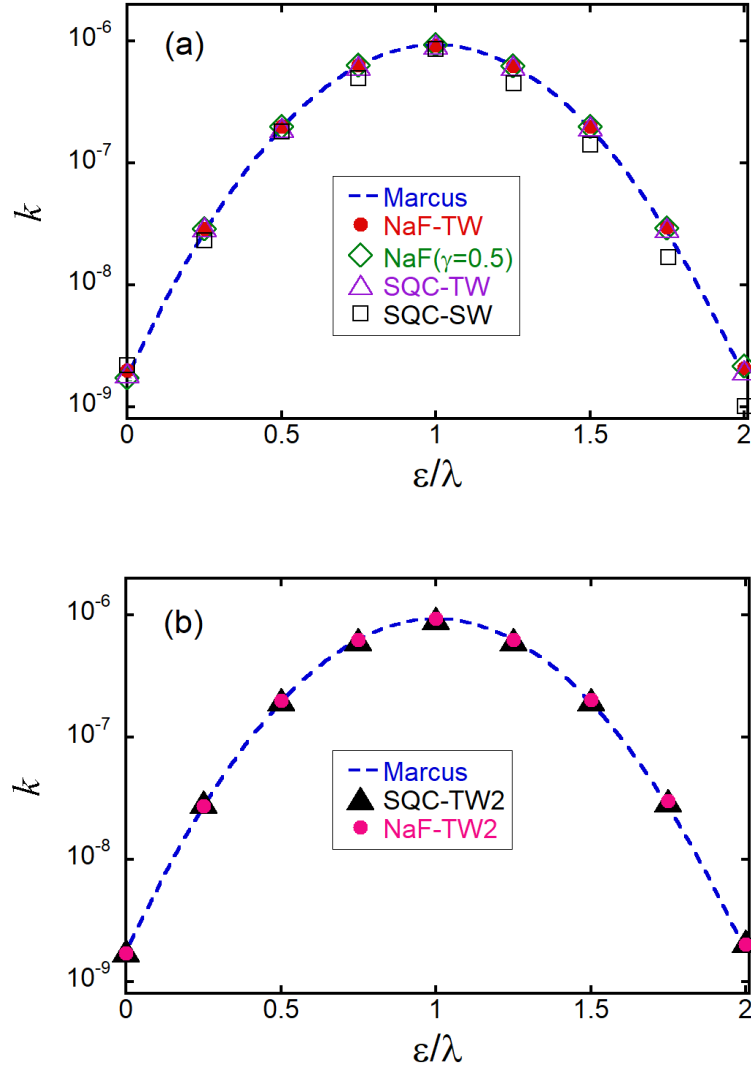
Figure S4. The electronic transfer rate k against ε / λ. In panel (a), blue dashed line, red points, green hollow diamonds and purple hollow triangles represent the results obtained from the Marcus theory, NaF-TW, NaF ($\gamma = 0.5$) and SQC-TW, respectively. Black hollow squares demonstrate the results of SQC with square window functions (denoted as SQC-SW in the figure) obtained from ref [53]. In panel (b), blue dashed line, black solid triangles and magenta points represent the results yielded from the Marcus theory, SQC-TW2 and NaF-TW2, respectively.

S4: Comparison of Different Strategies Employing Triangle Window Functions

For the SQC with triangle window functions, we compare two strategies. The first SQC-TW version as presented in the main text, involves the "trajectory-adjusted zero-point energy" treatment of the SQC-TW approach of Cotton and Miller in ref [4]. In this approach, we choose $\tilde{\rho}(t) = \frac{1}{2}\tilde{\mathbf{g}}_t\tilde{\mathbf{g}}_t^\dagger - \tilde{\Gamma}_0$ where (time-independent) commutator matrix $\tilde{\Gamma}$ is fixed during real-time evolution. In addition, we propose another version denoted as SQC-TW2, where we let $\tilde{\rho}(t) = \frac{1}{2}\tilde{\mathbf{g}}_t\tilde{\mathbf{g}}_t^\dagger - \tilde{\Gamma}_t$ and (time-dependent) commutator matrix $\tilde{\Gamma}$ evolves according to eq (S32). In Figures S5-S7, we present the comparison between SQC-TW and SQC-TW2 for three different types of models: the spin-boson model, the LVCM of the pyrazine molecule, and the FMO monomer model. The numerical performance of SQC-TW and that of SQC-TW2 do not differ much from each other in the model tests.
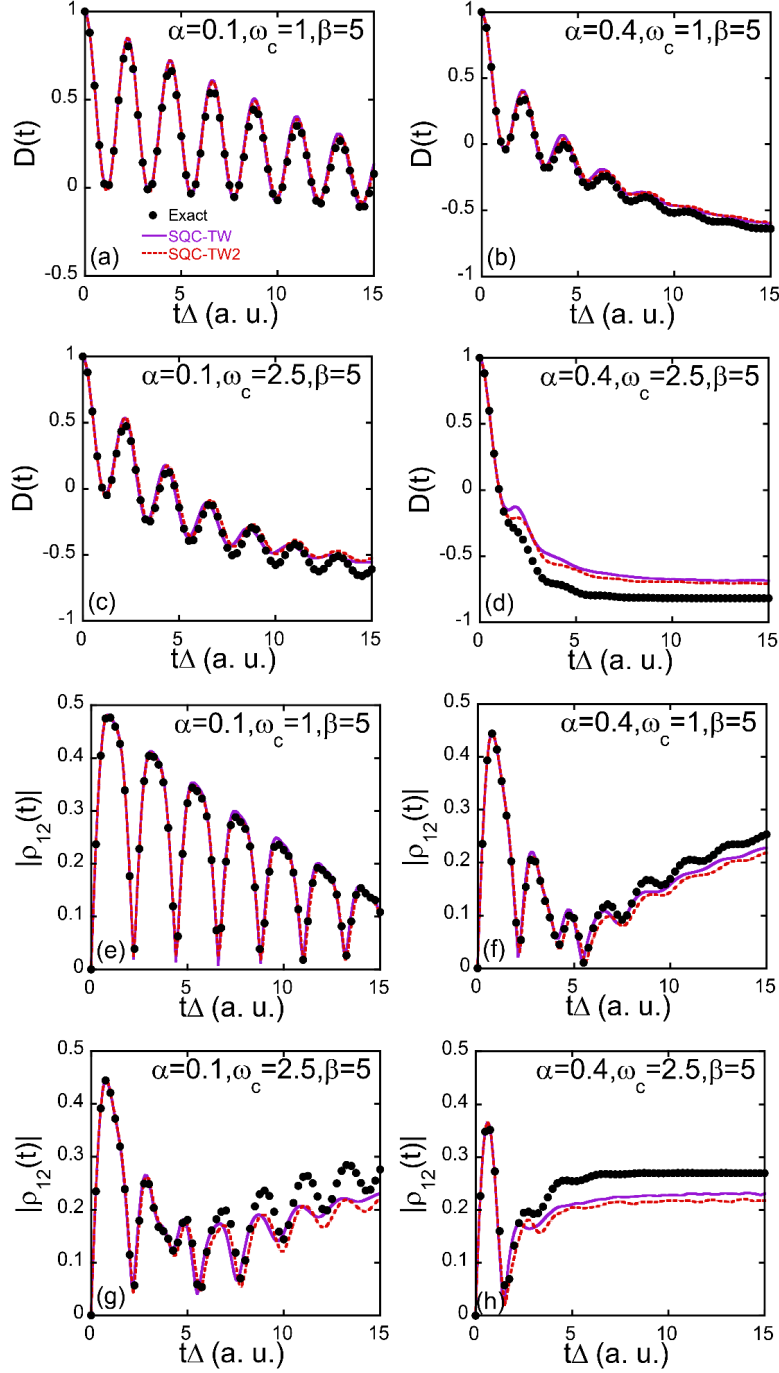
Figure S5. Comparison of the population dynamics (panels (a-d)) and coherence dynamics (panels (e-h)) of SQC-TW and those of SQC-TW2 for four spin-boson models discussed in the main text. The parameters for the models in panels (a-h) are consistent with those detailed in Figure 1 of the

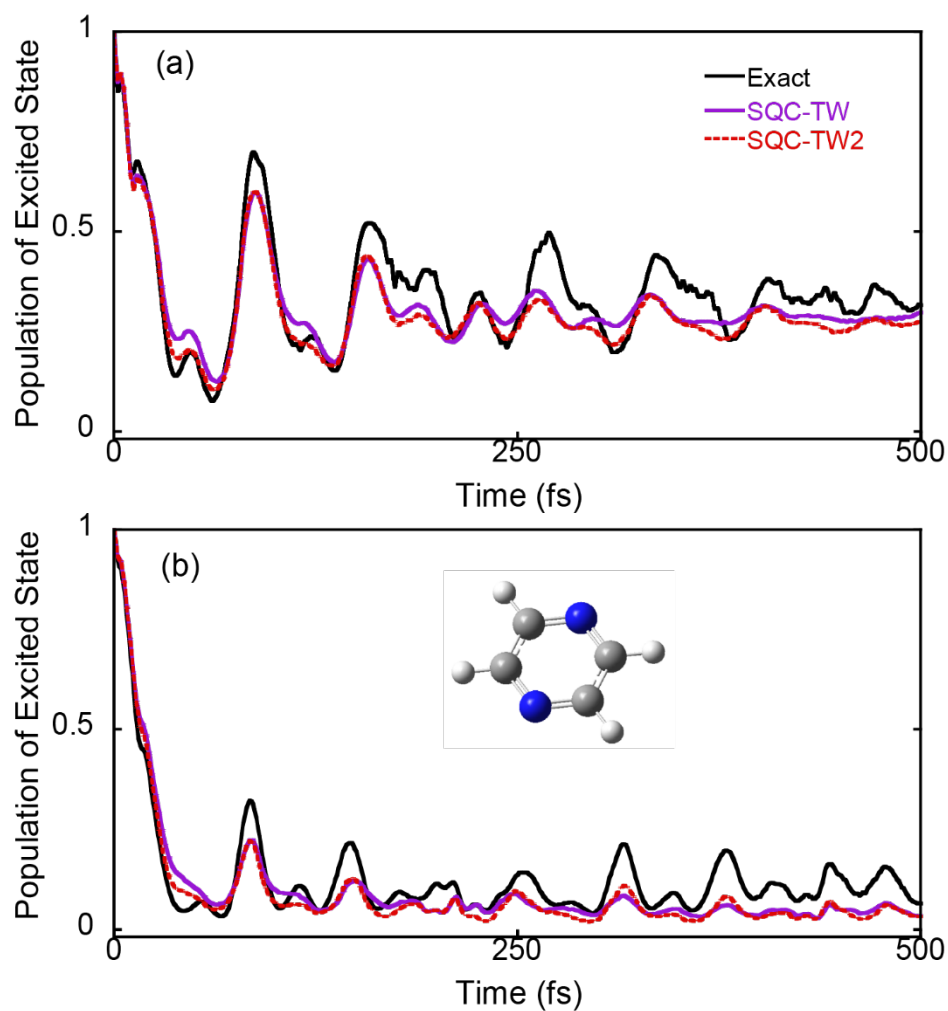main text. Purple lines: SQC-TW. Red dashed lines: SQC-TW2. Numerically exact results are denoted by black points.

Figure S6. Comparisons of SQC-TW and SQC-TW2 results. Panels (a-b) depict the population dynamics of the second state of the 2-state LVCM with 3 modes for pyrazine[47] and that with 24 modes for the same molecule[48], respectively. Purple lines: SQC-TW. Red dashed lines: SQC-TW2. Black lines: Numerically exact results produced by MCTDH [56].
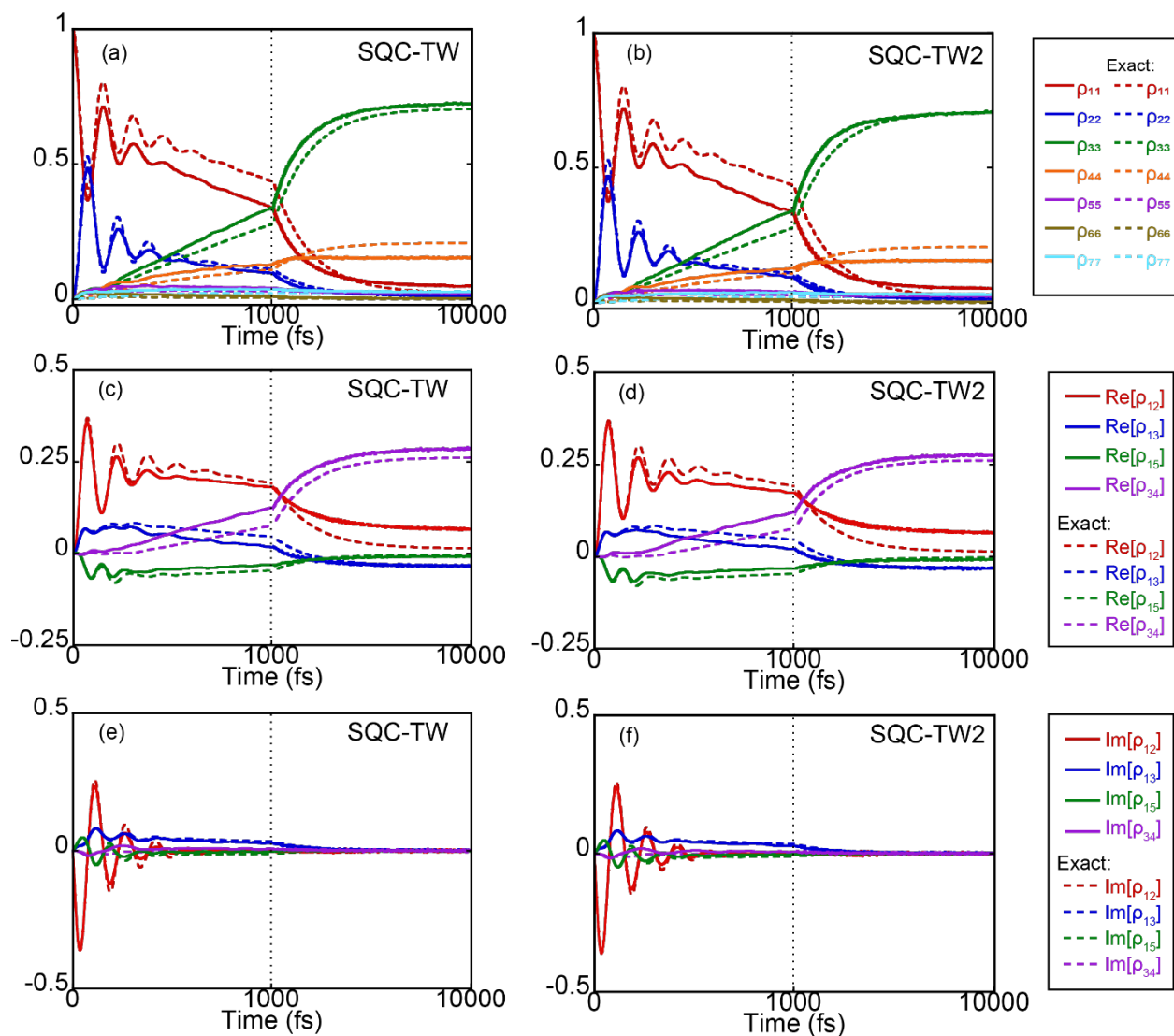
Figure S7. Comparisons of SQC-TW and SQC-TW2. Panels (a-b) depict the population dynamics of the FMO monomer reproduced by the SQC-TW and SQC-TW2, respectively. Panels (c-f) demonstrate the corresponding coherence dynamics of the FMO monomer for SQC-TW and SQC-TW2, respectively. The line colors in all panels match those used in Figure 2 of the main text.

We also compare two NaF-TW strategies. The first, as presented in the main text of the present paper, employs $\tilde{\rho}(t) = \left(1 + F/3\right)\tilde{\mathbf{g}}_t\tilde{\mathbf{g}}_t^\dagger / \mathrm{Tr}_e\left[\tilde{\mathbf{g}}_t\tilde{\mathbf{g}}_t^\dagger\right] - \mathbf{1}/3$. In the second approach, denoted as NaF-TW2, we alternatively employ $\tilde{\rho}(t) = \dfrac{1}{2}\tilde{\mathbf{g}}_t\tilde{\mathbf{g}}_t^\dagger - \tilde{\Gamma}_t$, where commutator matrix $\tilde{\Gamma}_t$ varies with time, and the sampling of initial value of $\tilde{\Gamma}_0$ is according to the details described in Sub-section S2-A. NaF-TW and NaF-TW2 exhibit nearly comparable performance across all benchmark models. In Figures S8-S12, we compare their performances in the spin-boson model, the LVCM of pyrazine molecule, the FMO monomer and Tully's models, respectively.
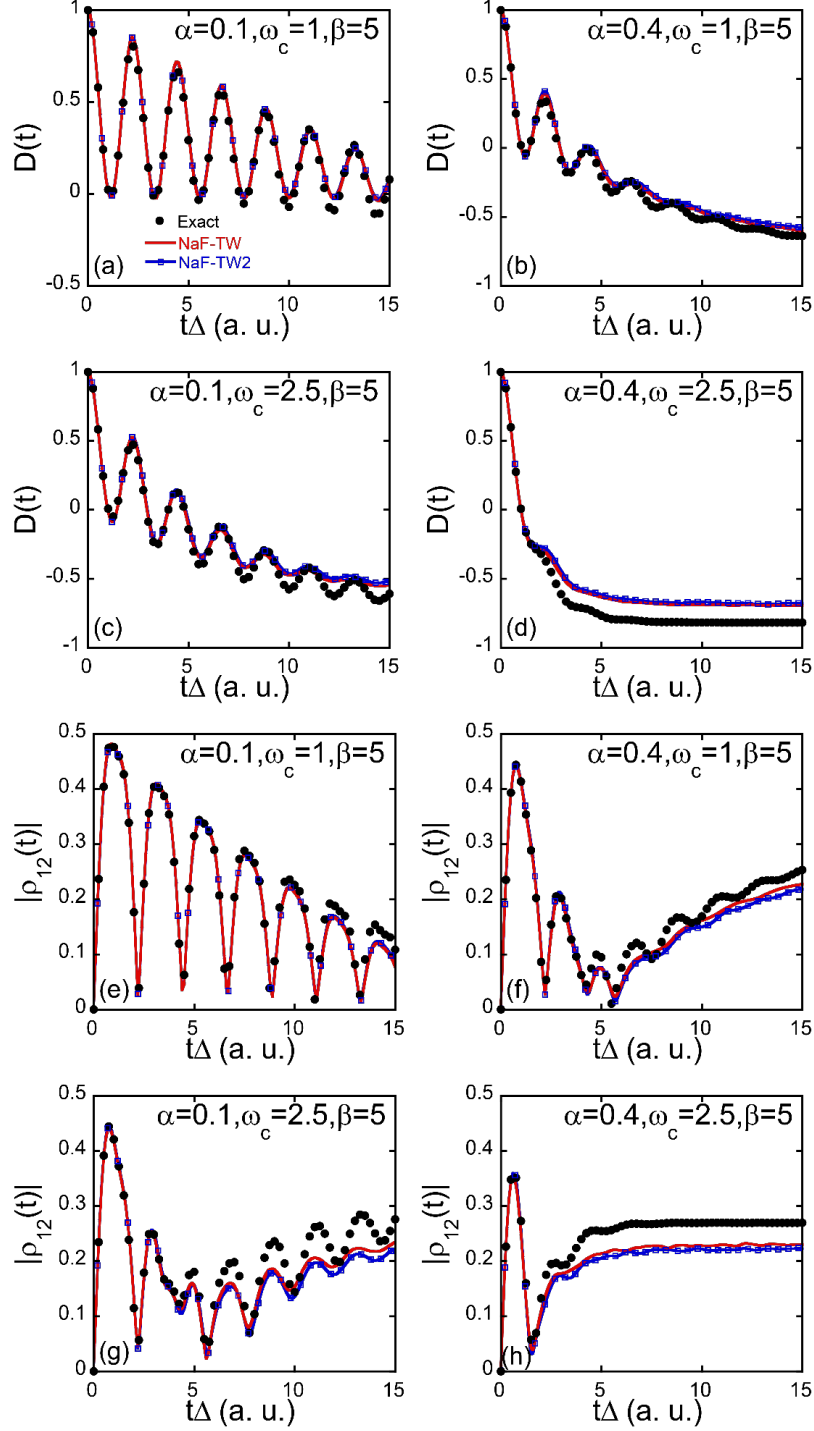
Figure S8. Comparison of the population dynamics (panels (a-d)) and coherence dynamics (panels (e-h)) of NaF-TW and NaF-TW2 for four spin-boson models discussed in the main text. The parameters for the models in panels (a-h) are consistent with those detailed in Figure 1 of the main

text. Red lines indicate: NaF-TW. Blue lines with hollow squares: NaF-TW2. Numerically exact results are denoted by black points.
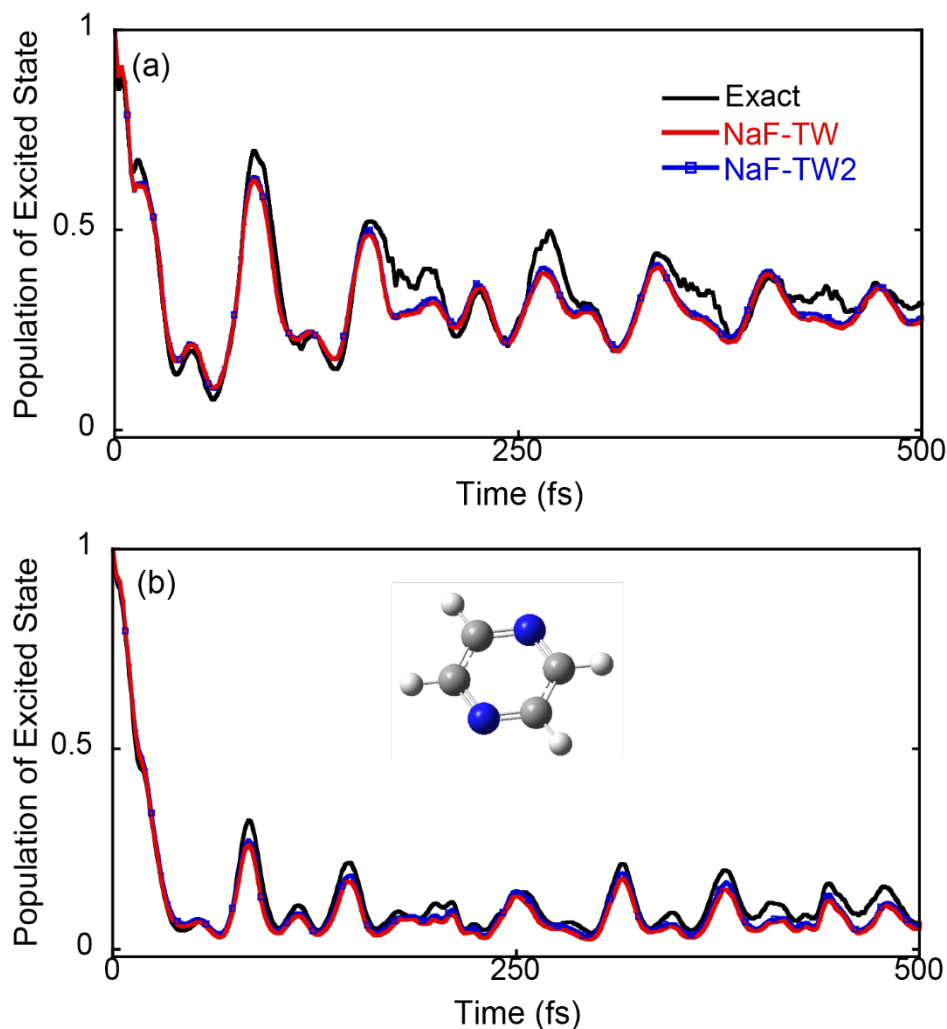

Figure S9. Comparisons of NaF-TW and NaF-TW2. Panels (a-b) depict the population dynamics of the second state of the 2-state LVCM with 3 modes for pyrazine [47] and that with 24 modes for the same molecule[48], respectively. Red lines: NaF-TW. Blue lines with hollow squares: NaF-TW2. Black lines: Numerically exact results produced by the MCTDH program[56].
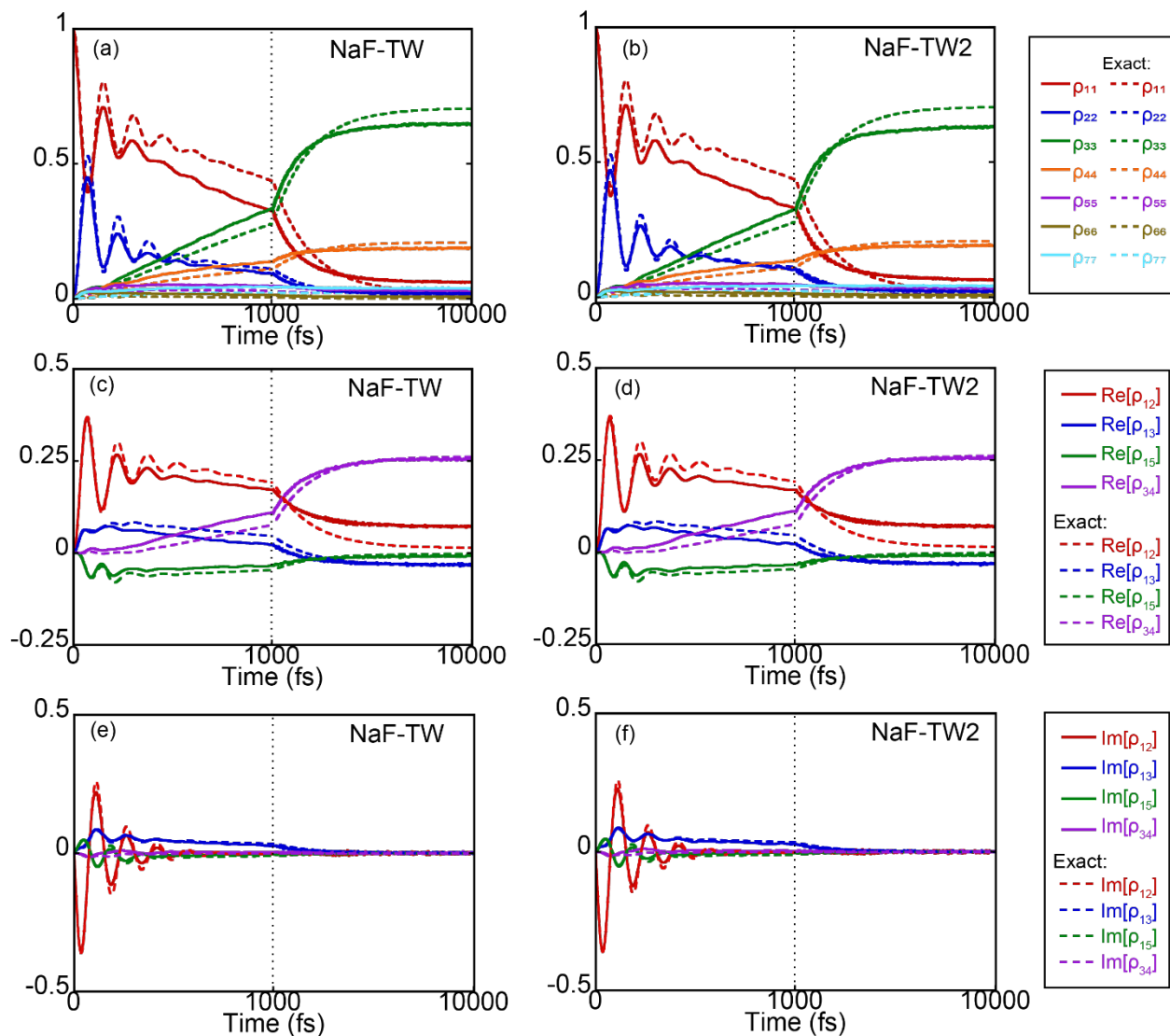
Figure S10. Comparisons of NaF-TW and NaF-TW2 results. Panels (a-b) depict the population dynamics of the FMO monomer as reproduced by the NaF-TW and NaF-TW2, respectively. Panels (c-f) show the corresponding coherence dynamics of the FMO monomer for the NaF-TW and NaF-TW2, respectively. The line colors in all panels match those used in Figure 2 of the main text.
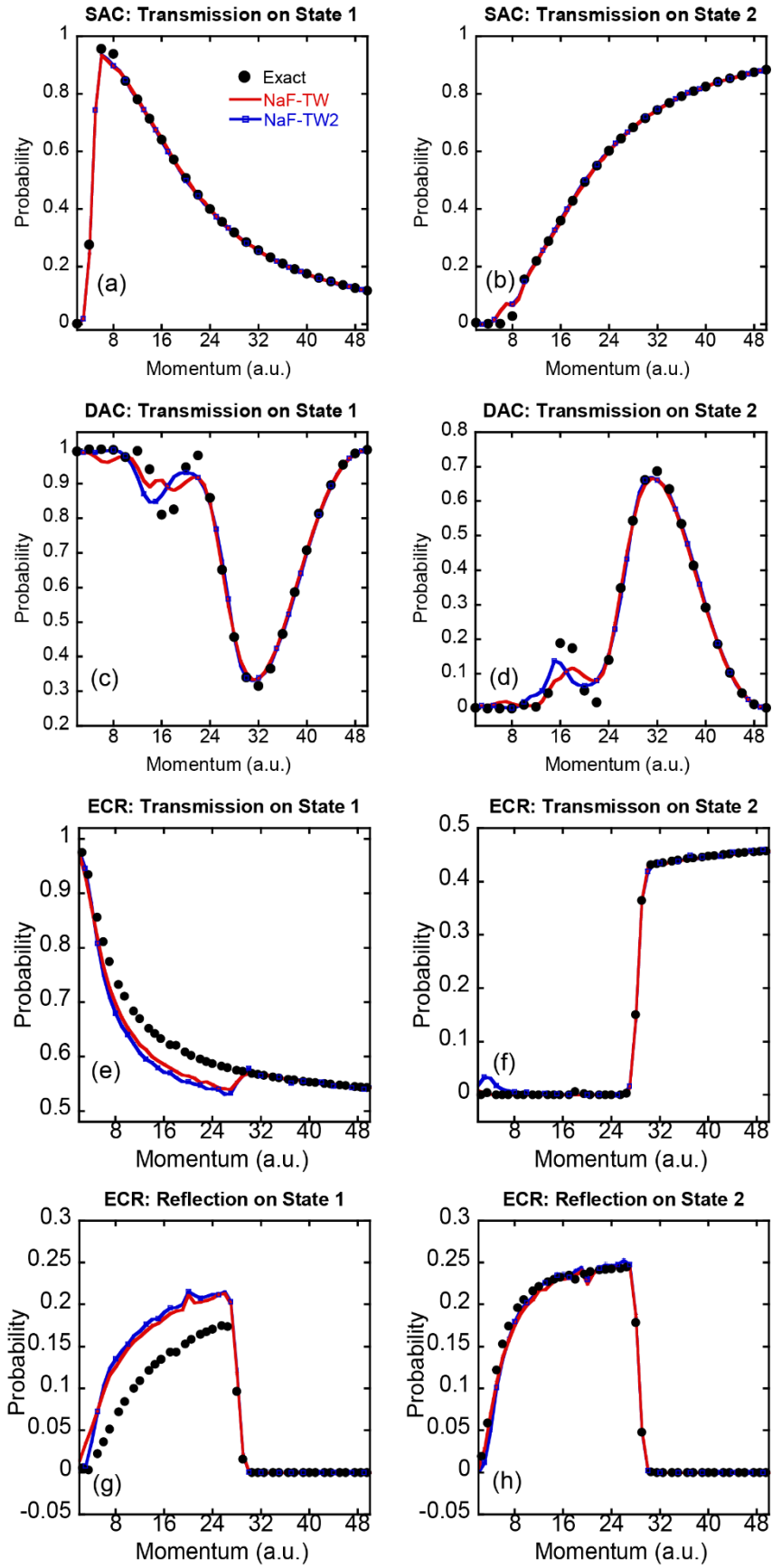
Figure S11. Comparisons of NaF-TW and NaF-TW2. Panels (a-b) depict the transmission probability on (adiabatic) State 1 and State 2 with respect to the center of momentum of the initial nuclear Gaussian wavepacket for Tully's SAC model, respectively. Panels (c-d) also show the transmission probability on (adiabatic) State 1 and State 2 but for Tully's DAC model. Panels (e-h) present the transmission probability on (adiabatic) State 1 and State 2, as well as the reflection probability on (adiabatic) State 1 and State 2 for Tully's ECR model, respectively. Red lines: NaF-TW. Blue lines with hollow squares: NaF-TW2. Black lines: Numerically exact results produced by DVR.
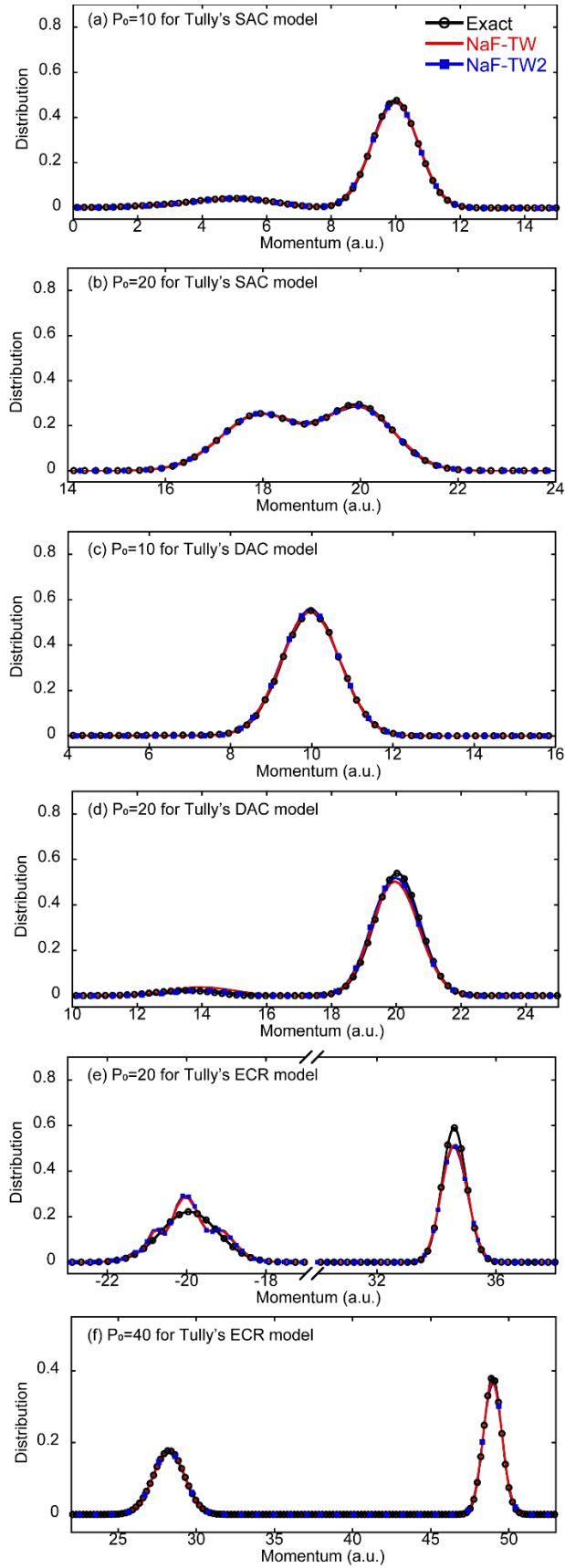
Legend:
- Exact
- NaF-TW
- NaF-TW2

(a) $P_0=10$ for Tully's SAC model

(b) $P_0=20$ for Tully's SAC model

(c) $P_0=10$ for Tully's DAC model

(d) $P_0=20$ for Tully's DAC model

(e) $P_0=20$ for Tully's ECR model

(f) $P_0=40$ for Tully's ECR model

Momentum (a.u.)

Distribution

S40

Figure S12. Comparisons of NaF-TW and NaF-TW2 results. Panels (a-b) depict the asymptotic nuclear momentum distribution for the initial momentum $P_0 = 10$ and $P_0 = 20$ of the center of the nuclear Gaussian wavepacket for Tully's SAC model, respectively. Panels (c-d) show the same distribution for the initial momentum $P_0 = 10$ and $P_0 = 20$ of the center of the nuclear Gaussian wavepacket for Tully's DAC model, respectively. Panels (e-f) present the same distribution for the initial momentum $P_0 = 20$ and $P_0 = 40$ of the center of the nuclear Gaussian wavepacket for Tully's ECR model, respectively. Red lines: NaF-TW. Blue lines with hollow squares: NaF-TW2. Black lines: Numerically exact results produced by DVR.

S5: Mapping Triangle Window Functions onto Constraint Phase Space Leads to Novel Phase Space Formulations for the *F*-state Quantum Systems

In this sub-section, we propose the phase space formulations on CPS which can be derived from the TW functions. Similar to Sub-section S1, consider an *F*-state discrete quantum system of electronic DOFs. Using action-angle variables, the expression of the population-population correlation function reads

$$\mathrm{Tr}_e\left[|n\rangle\langle n|e^{i\hat{H}t}|m\rangle\langle m|e^{-i\hat{H}t}\right] \mapsto \left(\overline{C}_{nn,mm}(t)\right)^{-1}p_{n\to m}^{\mathrm{SQC}}(t) , \tag{S59}$$

where

$$p_{n\to m}^{\mathrm{SQC}}(t) = \int \frac{2\mathrm{d}\mathbf{e}_0\mathrm{d}\boldsymbol{\theta}_0}{(2\pi)^F\left(2-e_0^{(n)}\right)^{F-2}}K_{nn}^{\mathrm{SQC}}\left(\mathbf{e}_0,\boldsymbol{\theta}_0\right)K_{mm}^{\mathrm{bin}}\left(\mathbf{e}_t,\boldsymbol{\theta}_t\right) \tag{S60}$$

and

$$\overline{C}_{nn,mm}(t) = \sum_{k=1}^{F} p_{n\to k}^{\mathrm{SQC}}(t) . \tag{S61}$$

In eq (S60), the definition of $K_{nn}^{\text{SQC}}(\mathbf{e}_0,\boldsymbol{\theta}_0)$ is the same as eq (S3); substituting eq (S1) into eqs (16)-(17) of the main text (of the present letter) leads to

$$K_{mm}^{\text{bin}}(\mathbf{e},\boldsymbol{\theta}) \equiv K_{mm}^{\text{bin}}(\mathbf{e}) = h\left(e^{(m)} - 1\right) \prod_{m' \neq m} h\left(1 - e^{(m')}\right). \tag{S62}$$

We then transform the integral on the action-angle space, eq (S60), to the integral counterpart on a single CPS. Because a phase space point at any time t always lies on a particular *iso-action* line $\sum_{n=1}^{F} e^{(n)} = \lambda$, the integral on the action space can be expressed as

$$\int_0^{+\infty} d\overline{e}^{(1)} \cdots d\overline{e}^{(F)} f\left(\overline{e}^{(1)},\cdots,\overline{e}^{(F)};\boldsymbol{\theta}\right)$$

$$= \int_0^{+\infty} d\overline{\lambda} \int_0^{+\infty} d\overline{e}^{(1)} \cdots d\overline{e}^{(F)} f\left(\overline{e}^{(1)},\cdots,\overline{e}^{(F)};\boldsymbol{\theta}\right) \delta\left(\sum_{n=1}^{F} \overline{e}^{(n)} - \overline{\lambda}\right) \tag{S63}$$

$$\overset{\overline{\lambda}=(1+F\gamma)\lambda}{\underset{\overline{e}^{(i)}=\lambda e^{(i)}}{=}} (1+F\gamma) \int_0^{+\infty} \lambda^{F-1} d\lambda \int_0^{+\infty} de^{(1)} \cdots de^{(F)} f\left(\lambda e^{(1)},\cdots,\lambda e^{(F)};\boldsymbol{\theta}\right) \delta\left(\sum_{n=1}^{F} e^{(n)} - (1+F\gamma)\right)$$

The transformation $\left\{\overline{e}_0^{(i)}\right\} \mapsto \left\{\lambda e_0^{(i)}\right\}$ leads to $\left\{\overline{e}_t^{(i)}\right\} \mapsto \left\{\lambda e_t^{(i)}\right\}$ at any time t. The integral of eq (S60) involved in the population-population correlation function can then be changed to

$$p_{n\rightarrow m}^{\text{SQC}}(t) = \int \frac{2d\mathbf{e}_0 d\boldsymbol{\theta}_0}{(2\pi)^F \left(2-e_0^{(n)}\right)^{F-2}} K_{nn}^{\text{SQC}}(\mathbf{e}_0) K_{mm}^{\text{bin}}(\mathbf{e}_t)$$

$$= \frac{(1+F\gamma)}{(2\pi)^F} \int F d\mathbf{e}_0 d\boldsymbol{\theta}_0 \delta\left(\sum_{k=1}^{F} e_0^{(k)} - (1+F\gamma)\right) \times$$

$$\int_0^{+\infty} \frac{2\lambda^{F-1}}{F\left(2-\lambda e_0^{(n)}\right)^{F-2}} d\lambda h\left(\lambda - \left(e_0^{(n)}\right)^{-1}\right) \prod_{n' \neq n} h\left(\frac{2}{e_0^{(n')} + e_0^{(n)}} - \lambda\right) \times \qquad , \tag{S64}$$

$$h\left(\lambda - \left(e_t^{(m)}\right)^{-1}\right) \prod_{m' \neq m} h\left(\left(e_t^{(m')}\right)^{-1} - \lambda\right)$$

$$= \frac{(1+F\gamma)}{(2\pi)^F} \int F d\mathbf{e}_0 d\boldsymbol{\theta}_0 \delta\left(\sum_{k=1}^{F} e_0^{(k)} - (1+F\gamma)\right) \overline{\Lambda}\left(\int_{h_1}^{h_2} \frac{2\lambda^{F-1}}{F\left(2-\lambda e_0^{(n)}\right)^{F-2}} d\lambda\right)$$

where the time-dependent boundaries h_1 and h_2 rely on the indexes, n and m,

$$h_1 = \max\left\{ \left(e_0^{(n)}\right)^{-1}, \left(e_t^{(m)}\right)^{-1} \right\},$$

$$h_2 = \min\left\{ \frac{2}{e_0^{(n')} + e_0^{(n)}}, \left(e_t^{(m')}\right)^{-1} \middle| n' \neq n,\, m' \neq m \right\}, \tag{S65}$$

and we define the function $\overline{\Lambda}(z) = \begin{cases} z, & \text{if } z > 0, \\ 0, & \text{otherwise} \end{cases}$. When $h_1 < h_2$ so that $p_{n \to m}^{\mathrm{SQC}}(t) \neq 0$, $e_t^{(m)} > e_t^{(m')}$

for any $m' \neq m$. In addition, at time 0 the n-th state is occupied, thus $e_0^{(n)} > e_0^{(n')}$ for any $n' \neq n$.

Since $\dfrac{2\lambda^{F-1}}{\left(2 - \lambda e_0^{(n)}\right)^{F-2}}$ monotonically increases as the value of λ does on the integration domain of

λ, we obtain the analytical integral

$$\overline{\Lambda}\left(\int_{h_1}^{h_2} \frac{2\lambda^{F-1}}{F\left(2 - \lambda e_0^{(n)}\right)^{F-2}}\, \mathrm{d}\lambda \right) = \frac{(F-1)!}{F} \prod_{n' \neq n} h\left(e_0^{(n)} - e_0^{(n')}\right) \prod_{m' \neq m} h\left(e_t^{(m)} - e_t^{(m')}\right) \times$$
$$\overline{\Lambda}\left(\phi\left(\min\left\{ \frac{2}{e_0^{(n')} + e_0^{(n)}}, \frac{1}{e_t^{(m')}} \middle| n' \neq n, m' \neq m \right\}; e_0^{(n)} \right) - \phi\left(\max\left\{ \frac{1}{e_0^{(n)}}, \frac{1}{e_t^{(m)}} \right\}; e_0^{(n)} \right) \right), \tag{S66}$$

where

$$\phi\left(\lambda; e^{(n)}\right) = \lambda^F \left(2 - \lambda e^{(n)}\right)^{1-F} \left[2(F-2)(F-1)\,{}_2\tilde{F}_1\left(1,1; F+1; \lambda e^{(n)}/2\right) + \frac{\left(6 - 2F - \lambda e^{(n)}\right)}{\Gamma(F)} \right]. \tag{S67}$$

Here, ${}_2\tilde{F}_1(a,b;c;z)$ is regularized hypergeometric function. Transforming eqs (S64)-(S67) back to

coordinate-momentum phase space variables, the population-population correlation function reads

$$\mathrm{Tr}\left[|n\rangle\langle n| e^{i\hat{H}t} |m\rangle\langle m| e^{-i\hat{H}t} \right] \mapsto \left(\overline{C}_{nn,mm}^{\mathrm{sqz}}(t) \right)^{-1} \int_{\mathcal{S}(\mathbf{x},\mathbf{p};\gamma)} F \mathrm{d}\mathbf{x}_0 \mathrm{d}\mathbf{p}_0 \, \overline{w}_{nn,mm}^{\mathrm{sqz}}\left(\mathbf{x}_0, \mathbf{p}_0; \mathbf{x}_t, \mathbf{p}_t \right)$$
$$\times K_{nn}^{\mathrm{sqz}}\left(\mathbf{x}_0, \mathbf{p}_0 \right) K_{mm}^{\mathrm{sqz}}\left(\mathbf{x}_t, \mathbf{p}_t \right), \tag{S68}$$

where $K_{nn}^{\mathrm{sqz}}(\mathbf{x},\mathbf{p}) \equiv K_{nn}^{\mathrm{sqz}}(\mathbf{e}, \boldsymbol{\theta}) = \prod_{n' \neq n} h\left(e^{(n)} - e^{(n')}\right)$. The time-dependent normalization factor is

$$\overline{C}_{nn,mm}^{\text{sqz}}(t) = \sum_{k=1}^{F} \int_{\mathcal{S}(\mathbf{x},\mathbf{p};\gamma)} F d\mathbf{x}_0 d\mathbf{p}_0 \overline{w}_{nn,kk}^{\text{sqz}} \left(\mathbf{x}_0, \mathbf{p}_0; \mathbf{x}_t, \mathbf{p}_t \right) K_{nn}^{\text{sqz}} \left(\mathbf{x}_0, \mathbf{p}_0 \right) K_{kk}^{\text{sqz}} \left(\mathbf{x}_t, \mathbf{p}_t \right) \tag{S69}$$

and the generalized weight function is

$$\overline{w}_{nn,mm}^{\text{sqz}} \left(\mathbf{x}_0, \mathbf{p}_0; \mathbf{x}_t, \mathbf{p}_t \right) \equiv \overline{w}_{nn,mm}^{\text{sqz}} \left(\mathbf{e}_0 \left(\mathbf{x}_0, \mathbf{p}_0 \right); \mathbf{e}_t \left(\mathbf{x}_t, \mathbf{p}_t \right) \right) = \frac{(1+F\gamma)^F}{F} \overline{\Lambda} \left(\tilde{z}_{nm} \left(\mathbf{e}_0, \mathbf{e}_t \right) \right) \tag{S70}$$

with

$$\tilde{z}_{nm} \left(\mathbf{e}_0, \mathbf{e}_t \right) = \phi \left(\min \left\{ \frac{2}{e_0^{(n' \neq n)} + e_0^{(n)}}, \frac{1}{e_t^{(m' \neq m)}} \middle| n' \neq n, m' \neq m \right\}; e_0^{(n)} \right) - \phi \left(\max \left\{ \frac{1}{e_0^{(n)}}, \frac{1}{e_t^{(m)}} \right\}; e_0^{(n)} \right) \tag{S71}$$

for general F-state systems, which depends on both the values of $\mathbf{e}_0 \left(\mathbf{x}_0, \mathbf{p}_0 \right)$ and those of

$\mathbf{e}_t \left(\mathbf{x}_t, \mathbf{p}_t \right)$. We denoted it as the squeezed (sqz) triangular window function approach. In this

approach, the initial sampling is on the $\text{U}(F)/\text{U}(F-1)$ CPS, $\mathcal{S}(\mathbf{x}, \mathbf{p}; \gamma)$. The approach involves

a time-dependent normalization factor for the population-population correlation function. The

population-population correlation function of the sqz triangular window function approach is

identical to that using TW functions for electronic DOFs of the F-state system.

Particularly, for the case of $F = 2$, it is straightforward to derive $\phi \left(\lambda; e^{(n)} \right) = \lambda^2$.

Correspondingly, $\overline{w}_{nn,mm}^{\text{sqz}} \left(\mathbf{x}_0, \mathbf{p}_0; \mathbf{x}_t, \mathbf{p}_t \right) \equiv \overline{w}_{nn,mm}^{\text{sqz}} \left(\mathbf{e}_0 \left(\mathbf{x}_0, \mathbf{p}_0 \right); \mathbf{e}_t \left(\mathbf{x}_t, \mathbf{p}_t \right) \right) = 2 - \frac{(1+F\gamma)^2}{2 \min \left\{ e_0^{(n)}, e_t^{(m)} \right\}^2}$.

The $F = 2$ case of the sqz formalism is used in the proof that the mapping formalism with TW

functions offers an *exact* representation for the population dynamics for the pure two-state system

(TSS), as demonstrated in our work of ref [1].

■ AUTHOR INFORMATION

Corresponding Author

*E-mail: jianliupku@pku.edu.cn

ORCID

Xin He: 0000-0002-5189-7204

Xiangsong Cheng: 0000-0001-8793-5092

Baihua Wu: 0000-0002-1256-6859

Jian Liu: 0000-0002-2906-5858

Notes

The authors declare no competing financial interests.

■ REFERENCES

(1)   Cheng, X.; He, X.; Liu, J., A Novel Class of Phase Space Representations for the Exact Population Dynamics of Two-State Quantum Systems and the Relation to Symmetrical Window Functions. *Chinese J. Chem. Phys.* **2024**, *37*, 230-254. http://dx.doi.org/10.1063/1674-0068/cjcp2403033

(2)   Cotton, S. J.; Miller, W. H., A Symmetrical Quasi-Classical Windowing Model for the Molecular Dynamics Treatment of Non-Adiabatic Processes Involving Many Electronic States. *J. Chem. Phys.* **2019**, *150*, 104101. http://dx.doi.org/10.1063/1.5087160

(3)   He, X.; Wu, B.; Shang, Y.; Li, B.; Cheng, X.; Liu, J., New Phase Space Formulations and Quantum Dynamics Approaches. *Wiley Interdiscip. Rev. Comput. Mol. Sci.* **2022**, *12*, e1619. http://dx.doi.org/10.1002/wcms.1619

(4)   Cotton, S. J.; Miller, W. H., Trajectory-Adjusted Electronic Zero Point Energy in Classical Meyer-Miller Vibronic Dynamics: Symmetrical Quasiclassical Application to Photodissociation. *J. Chem. Phys.* **2019**, *150*, 194110. http://dx.doi.org/10.1063/1.5094458

(5)   Tully, J. C.; Preston, R. K., Trajectory Surface Hopping Approach to Nonadiabatic Molecular Collisions: The Reaction of H^+ with D_2. *J. Chem. Phys.* **1971**, *55*, 562-572. http://dx.doi.org/10.1063/1.1675788

(6)   Tully, J. C., Molecular Dynamics with Electronic Transitions. *J. Chem. Phys.* **1990**, *93*, 1061-1071. http://dx.doi.org/10.1063/1.459170

(7)   Wu, B.; He, X.; Liu, J., Nonadiabatic Field on Quantum Phase Space: A Century after Ehrenfest. *J. Phys. Chem. Lett.* **2024**, *15*, 644-658. http://dx.doi.org/10.1021/acs.jpclett.3c03385

(8)   Makarov, D. E.; Makri, N., Path Integrals for Dissipative Systems by Tensor Multiplication. Condensed Phase Quantum Dynamics for Arbitrarily Long Time. *Chem. Phys. Lett.* **1994**, *221*, 482-491. http://dx.doi.org/10.1016/0009-2614(94)00275-4

(9)   Makri, N.; Makarov, D. E., Tensor Propagator for Iterative Quantum Time Evolution of Reduced Density Matrices. II. Numerical Methodology. *J. Chem. Phys.* **1995**, *102*, 4611-4618. http://dx.doi.org/10.1063/1.469509

(10)   Makri, N.; Makarov, D. E., Tensor Propagator for Iterative Quantum Time Evolution of Reduced Density Matrices. I. Theory. *J. Chem. Phys.* **1995**, *102*, 4600-4610. http://dx.doi.org/10.1063/1.469508

(11)   Makri, N., Small Matrix Path Integral with Extended Memory. *J. Chem. Theory. Comput.* **2021**, *17*, 1-6. http://dx.doi.org/10.1021/acs.jctc.0c00987

(12)   Makri, N., Small Matrix Disentanglement of the Path Integral: Overcoming the Exponential Tensor Scaling with Memory Length. *J. Chem. Phys.* **2020**, *152*, 041104. http://dx.doi.org/10.1063/1.5139473

(13)   Tanimura, Y.; Kubo, R., Time Evolution of a Quantum System in Contact with a Nearly Gaussian-Markoffian Noise Bath. *J. Phys. Soc. Jpn.* **1989**, *58*, 101-114. http://dx.doi.org/10.1143/JPSJ.58.101

(14)   Yan, Y.-A.; Yang, F.; Liu, Y.; Shao, J., Hierarchical Approach Based on Stochastic Decoupling to Dissipative Systems. *Chem. Phys. Lett.* **2004**, *395*, 216-221. http://dx.doi.org/10.1016/j.cplett.2004.07.036

(15)   Xu, R.-X.; Cui, P.; Li, X.-Q.; Mo, Y.; Yan, Y., Exact Quantum Master Equation Via the Calculus on Path Integrals. *J. Chem. Phys.* **2005**, *122*, 041103. http://dx.doi.org/10.1063/1.1850899

(16)   Shao, J., Stochastic Description of Quantum Open Systems: Formal Solution and Strong Dissipation Limit. *Chem. Phys.* **2006**, *322*, 187-192. http://dx.doi.org/10.1016/j.chemphys.2005.08.007

(17)   Moix, J. M.; Cao, J., A Hybrid Stochastic Hierarchy Equations of Motion Approach to Treat the Low Temperature Dynamics of Non-Markovian Open Quantum Systems. *J. Chem. Phys.* **2013**, *139*, 134106. http://dx.doi.org/10.1063/1.4822043

(18)   Meyer, H.-D.; Manthe, U.; Cederbaum, L. S., The Multi-Configurational Time-Dependent Hartree Approach. *Chem. Phys. Lett.* **1990**, *165*, 73-78. http://dx.doi.org/10.1016/0009-2614(90)87014-i

(19)   Thoss, M.; Wang, H.; Miller, W. H., Self-Consistent Hybrid Approach for Complex Systems: Application to the Spin-Boson Model with Debye Spectral Density. *J. Chem. Phys.* **2001**, *115*, 2991-3005. http://dx.doi.org/10.1063/1.1385562

(20)   Wang, H.; Thoss, M., Multilayer Formulation of the Multiconfiguration Time-Dependent Hartree Theory. *J. Chem. Phys.* **2003**, *119*, 1289-1299. http://dx.doi.org/10.1063/1.1580111

(21)   Ren, J. J.; Li, W. T.; Jiang, T.; Wang, Y. H.; Shuai, Z. G., Time-Dependent Density Matrix Renormalization Group Method for Quantum Dynamics in Complex Systems. *Wiley Interdiscip. Rev. Comput. Mol. Sci.* **2022**, *12*, e1614. http://dx.doi.org/10.1002/wcms.1614

(22)   Makri, N., The Linear Response Approximation and Its Lowest Order Corrections: An Influence Functional Approach. *J. Phys. Chem. B* **1999**, *103*, 2823-2829. http://dx.doi.org/10.1021/jp9847540

(23)   Wang, H., Iterative Calculation of Energy Eigenstates Employing the Multilayer Multiconfiguration Time-Dependent Hartree Theory. *J. Phys. Chem. A* **2014**, *118*, 9253-9261. http://dx.doi.org/10.1021/jp503351t

(24)   He, X.; Gong, Z.; Wu, B.; Liu, J., Negative Zero-Point-Energy Parameter in the Meyer-Miller Mapping Model for Nonadiabatic Dynamics. *J. Phys. Chem. Lett.* **2021**, *12*, 2496-2501. http://dx.doi.org/10.1021/acs.jpclett.1c00232

(25)   Fenna, R. E.; Matthews, B. W., Chlorophyll Arrangement in a Bacteriochlorophyll Protein from Chlorobium-Limicola. *Nature* **1975**, *258*, 573-577. http://dx.doi.org/10.1038/258573a0

(26)   Engel, G. S.; Calhoun, T. R.; Read, E. L.; Ahn, T. K.; Mancal, T.; Cheng, Y. C.; Blankenship, R. E.; Fleming, G. R., Evidence for Wavelike Energy Transfer through Quantum Coherence in Photosynthetic Systems. *Nature* **2007**, *446*, 782-786. http://dx.doi.org/10.1038/nature05678

(27)   Maiuri, M.; Ostroumov, E. E.; Saer, R. G.; Blankenship, R. E.; Scholes, G. D., Coherent Wavepackets in the Fenna-Matthews-Olson Complex Are Robust to Excitonic-Structure Perturbations Caused by Mutagenesis. *Nat. Chem.* **2018**, *10*, 177-183. http://dx.doi.org/10.1038/Nchem.2910

(28)   Higgins, J. S.; Lloyd, L. T.; Sohail, S. H.; Allodi, M. A.; Otto, J. P.; Saer, R. G.; Wood, R. E.; Massey, S. C.; Ting, P. C.; Blankenship, R. E., et al., Photosynthesis Tunes Quantum-Mechanical Mixing of Electronic and Vibrational States to Steer Exciton Energy Transfer. *Proc. Natl. Acad. Sci.* **2021**, *118*, e2018240118. http://dx.doi.org/10.1073/pnas.2018240118

(29)   Ishizaki, A.; Fleming, G. R., Theoretical Examination of Quantum Coherence in a Photosynthetic System at Physiological Temperature. *Proc. Natl. Acad. Sci.* **2009**, *106*, 17255-17260. http://dx.doi.org/10.1073/pnas.0908989106

(30)   Tao, G.; Miller, W. H., Semiclassical Description of Electronic Excitation Population Transfer in a Model Photosynthetic System. *J. Phys. Chem. Lett.* **2010**, *1*, 891-894. http://dx.doi.org/10.1021/jz1000825

(31)   Miller, W. H., Perspective: Quantum or Classical Coherence? *J. Chem. Phys.* **2012**, *136*, 210901. http://dx.doi.org/10.1063/1.4727849

(32)   Cao, J. S.; Cogdell, R. J.; Coker, D. F.; Duan, H. G.; Hauer, J.; Kleinekathofer, U.; Jansen, T. L. C.; Mancal, T.; Miller, R. J. D.; Ogilvie, J. P., et al., Quantum Biology Revisited. *Sci. Adv.* **2020**, *6*, eaaz4888. http://dx.doi.org/10.1126/sciadv.aaz4888

(33) Wang, H.; Song, X.; Chandler, D.; Miller, W. H., Semiclassical Study of Electronically Nonadiabatic Dynamics in the Condensed-Phase: Spin-Boson Problem with Debye Spectral Density. *J. Chem. Phys.* **1999**, *110*, 4828-4840. http://dx.doi.org/10.1063/1.478388

(34) Craig, I. R.; Thoss, M.; Wang, H., Proton Transfer Reactions in Model Condensed-Phase Environments: Accurate Quantum Dynamics Using the Multilayer Multiconfiguration Time-Dependent Hartree Approach. *J. Chem. Phys.* **2007**, *127*, 144503. http://dx.doi.org/10.1063/1.2772265

(35) He, X.; Wu, B.; Gong, Z.; Liu, J., Commutator Matrix in Phase Space Mapping Models for Nonadiabatic Quantum Dynamics. *J. Phys. Chem. A* **2021**, *125*, 6845-6863. http://dx.doi.org/10.1021/acs.jpca.1c04429

(36) Liu, J.; Miller, W. H., A Simple Model for the Treatment of Imaginary Frequencies in Chemical Reaction Rates and Molecular Liquids. *J. Chem. Phys.* **2009**, *131*, 074113. http://dx.doi.org/10.1063/1.3202438

(37) Duan, C. R.; Tang, Z. F.; Cao, J. S.; Wu, J. L., Zero-Temperature Localization in a Sub-Ohmic Spin-Boson Model Investigated by an Extended Hierarchy Equation of Motion. *Phys. Rev. B* **2017**, *95*, 214308. http://dx.doi.org/10.1103/PhysRevB.95.214308

(38) Tang, Z.; Ouyang, X.; Gong, Z.; Wang, H.; Wu, J., Extended Hierarchy Equation of Motion for the Spin-Boson Model. *J. Chem. Phys.* **2015**, *143*, 224112. http://dx.doi.org/10.1063/1.4936924

(39) Haugland, T. S.; Ronca, E.; Kjønstad, E. F.; Rubio, A.; Koch, H., Coupled Cluster Theory for Molecular Polaritons: Changing Ground and Excited States. *Phys. Rev. X* **2020**, *10*, 041043. http://dx.doi.org/10.1103/PhysRevX.10.041043

(40) Garcia-Vidal, F. J.; Ciuti, C.; Ebbesen, T. W., Manipulating Matter by Strong Coupling to Vacuum Fields. *Science* **2021**, *373*, eabd0336. http://dx.doi.org/10.1126/science.abd0336

(41) Toida, H.; Nakajima, T.; Komiyama, S., Vacuum Rabi Splitting in a Semiconductor Circuit QED System. *Phys. Rev. Lett.* **2013**, *110*, 066802. http://dx.doi.org/10.1103/PhysRevLett.110.066802

(42) Guerin, W.; Santo, T.; Weiss, P.; Cipris, A.; Schachenmayer, J.; Kaiser, R.; Bachelard, R., Collective Multimode Vacuum Rabi Splitting. *Phys. Rev. Lett.* **2019**, *123*, 243401. http://dx.doi.org/10.1103/PhysRevLett.123.243401

(43) Hoffmann, N. M.; Schafer, C.; Rubio, A.; Kelly, A.; Appel, H., Capturing Vacuum Fluctuations and Photon Correlations in Cavity Quantum Electrodynamics with Multitrajectory Ehrenfest Dynamics. *Phys. Rev. A* **2019**, *99*, 063819. http://dx.doi.org/10.1103/PhysRevA.99.063819

(44) Hoffmann, N. M.; Schäfer, C.; Säkkinen, N.; Rubio, A.; Appel, H.; Kelly, A., Benchmarking Semiclassical and Perturbative Methods for Real-Time Simulations of Cavity-Bound Emission and Interference. *J. Chem. Phys.* **2019**, *151*, 244113. http://dx.doi.org/10.1063/1.5128076

(45) Li, T. E.; Chen, H. T.; Nitzan, A.; Subotnik, J. E., Quasiclassical Modeling of Cavity Quantum Electrodynamics. *Phys. Rev. A* **2020**, *101*, 033831. http://dx.doi.org/10.1103/PhysRevA.101.033831

(46) Saller, M. A. C.; Kelly, A.; Geva, E., Benchmarking Quasiclassical Mapping Hamiltonian Methods for Simulating Cavity-Modified Molecular Dynamics. *J. Phys. Chem. Lett.* **2021**, *12*, 3163-3170. http://dx.doi.org/10.1021/acs.jpclett.1c00158

(47)   Schneider, R.; Domcke, W., S_1-S_2 Conical Intersection and Ultrafast S_2->S_1 Internal Conversion in Pyrazine. *Chem. Phys. Lett.* **1988**, *150*, 235-242. http://dx.doi.org/10.1016/0009-2614(88)80034-4

(48)   Krempl, S.; Winterstetter, M.; Plöhn, H.; Domcke, W., Path-Integral Treatment of Multi-Mode Vibronic Coupling. *J. Chem. Phys.* **1994**, *100*, 926-937. http://dx.doi.org/10.1063/1.467253

(49)   Worth, G. A.; Welch, G.; Paterson, M. J., Wavepacket Dynamics Study of $Cr(CO)_5$ after Formation by Photodissociation: Relaxation through an (E $\oplus$ A) $\otimes$ e Jahn–Teller Conical Intersection. *Mol. Phys.* **2006**, *104*, 1095-1105. http://dx.doi.org/10.1080/00268970500418182

(50)   Coronado, E. A.; Xing, J.; Miller, W. H., Ultrafast Non-Adiabatic Dynamics of Systems with Multiple Surface Crossings: A Test of the Meyer-Miller Hamiltonian with Semiclassical Initial Value Representation Methods. *Chem. Phys. Lett.* **2001**, *349*, 521-529. http://dx.doi.org/10.1016/s0009-2614(01)01242-8

(51)   Colbert, D. T.; Miller, W. H., A Novel Discrete Variable Representation for Quantum Mechanical Reactive Scattering Via the S-Matrix Kohn Method. *J. Chem. Phys.* **1992**, *96*, 1982-1991. http://dx.doi.org/10.1063/1.462100

(52)   Huo, P.; Miller, T. F.; Coker, D. F., Communication: Predictive Partial Linearized Path Integral Simulation of Condensed Phase Electron Transfer Dynamics. *J. Chem. Phys.* **2013**, *139*, 151103. http://dx.doi.org/10.1063/1.4826163

(53)   Cotton, S. J.; Igumenshchev, K.; Miller, W. H., Symmetrical Windowing for Quantum States in Quasi-Classical Trajectory Simulations: Application to Electron Transfer. *J. Chem. Phys.* **2014**, *141*, 084104. http://dx.doi.org/10.1063/1.4893345

(54)   Miller, W. H.; Schwartz, S. D.; Tromp, J. W., Quantum-Mechanical Rate Constants for Bimolecular Reactions. *J. Chem. Phys.* **1983**, *79*, 4889-4898. https://dx.doi.org/10.1063/1.445581

(55)   Marcus, R. A., On the Theory of Electron-Transfer Reactions. VI. Unified Treatment for Homogeneous and Electrode Reactions. *J. Chem. Phys.* **1965**, *43*, 679-701. http://dx.doi.org/10.1063/1.1696792

(56)   Worth, G. A.; Beck, M. H.; Jackle, A.; Meyer, H.-D. The MCTDH Package, Version 8.2, (2000). H.-D. Meyer, Version 8.3 (2002), Version 8.4 (2007). O. Vendrell and H.-D. Meyer Version 8.5 (2013). Version 8.5 contains the ML-MCTDH algorithm. See http://mctdh.uni-hd.de. (accessed on November 1st, 2023) Used version: 8.5.14.